ABSTRACT

ESTRICH, NICOLE ASHLEY. Gallium-Doped Zinc Oxide as a Conductive Antireflection Coating for Silicon Solar Cell Applications. (Under the direction of Dr. Jon-Paul Maria.)

Solar cell technology has gained much in efficiency through the use of antireflection coatings (ARCs). Common ARCs for silicon solar cells such as SiN_x are insulating, either requiring an additional layer, a transparent conductive layer, or a fired-through step to allow top contacts to etch through the insulating layer to reach the semiconducting layer below. Gallium-doped zinc oxide (GZO) presents the possibility of maintaining a conductive antireflection layer and thus increasing overall efficiency.

This thesis reports an evaluation of transparent, conductive gallium-doped ZnO thin films for a conducting antireflection coating appropriate for crystalline silicon solar cells as a means to enhance efficiency by reducing the overall resistivity of the photovoltaic circuit. All Ga-doped ZnO thin films in this study were deposited using pulsed laser deposition. The structural, electrical and optical properties of the as-grown GZO films were investigated, as well as contact resistance of silver contacts to the GZO thin films using the circular transmission line method (CTLM). The effects of thermal annealing were examined. In X-ray diffraction, the (002) peak was detected, indicating that Ga doping did not cause structural degradation of wurtzite ZnO. A visible transmittance of above 90% was obtained using UV-vis spectrometry. The lowest electrical resistivity values found via the Hall method were 8.5×10^{-4} Ohm-cm, with

carrier concentration of -2.8x10^{15} cm^{-3} and carrier mobility of 2.6 cm^2/V-s for GZO deposited at an oxygen pressure of 5mT, on an insulating surface.

Optimized films were next prepared on reference flat silicon wafers with known dopant densities and on commercially available solar cell substrates and patterned for circular transmission line method (CTLM) measurements of specific contact resistivity ρ_c. For textured *n*-emitter cells, contact resistivity values of 2 mohm-cm^2 were observed routinely. These values are consistent with, or lower than contact resistivities associated with conventional silver-based metallization.

Prototype cells were then fabricated, including ARC as well as top and bottom contacts. Efficiency measurements were made on these cells to provide a first look at cell performance.

Gallium-Doped Zinc Oxide as a Conductive Antireflection Coating for Silicon Solar Cell Applications

by
Nicole Ashley Estrich

A thesis submitted to the Graduate Faculty of
North Carolina State University
in partial fulfillment of the
requirements for the Degree of
Master of Science

Materials Science and Engineering

Raleigh, North Carolina

2012

APPROVED BY:

_____	_____
Michael Dickey	James LeBeau

_____
Jon-Paul Maria
Chair of Advisory Committee

BIOGRAPHY

Nicole Ashley Estrich was born on June 23, 1988 to parents Scott and Pamela Estrich in Raleigh, North Carolina. Though born and raised in the south, the influence of her New Yorker family has stuck with her. Following a happy childhood in which she already had a keen interest in mathematics, Nicole discovered the wonders of physics at Broughton High School.

Next, Nicole attended the University of North Carolina at Chapel Hill to see where her new love for physics would take her. Nicole spent a summer at Bucknell University studying the lifetime of positronium decay, and had great fun with all the electronics and filters. When back at UNC, Nicole spent a year doing optics research for the benefit of cancer research. In 2010, Nicole completed her Bachelor's of Science in Physics with a minor in Mathematics. From her research experience, Nicole knew that she wanted to pursue an education with focus on applied engineering.

Just one month later, Nicole joined Dr. Maria's group at North Carolina State University in the department of Materials Science & Engineering. With any change in subject, there are always new things to learn and new ideas around which one may wrap her head. Nicole is nearly certain that, though she will not try, she could likely operate a laser with her eyes shut. Nicole successfully defended her Master's thesis on August 10th, 2012.

ACKNOWLEDGMENTS

Many thanks are in order. Firstly, a big thanks to Dr. Jon-Paul Maria for providing all of his students with top-notch equipment and an incredible environment in which to thrive and grow. Also, Dr. Brian J. Laughlin, my industrial mentor at DuPont Electronics, for his expertise and most helpful guidance. Thank you to Mr. Joe Matthews in the clean room, and to committee member Dr. Michael Dickey for helping me pursue my lithographic interests. Thank you to Andy Xie and Wei Guo for your time on the UV-vis. Also, a big thanks to committee member Dr. James LeBeau. And Edna Deas, you are everyone's savior.

Of course, a thank you to all current and past group members, whose additional brains made brainstorming that much more productive, as well as providing friendship in and out of the lab: Peter Lam, Michelle Casper, Beth Paisley, David Hook (David 1), David Harris (David Also), Edward J. Mily, Alex Smith, Edward Sachet, Chris Shelton, William Luke, and Xiao Yu Kang.

Nothing is possible without the help and support of a family. I'm forever grateful for my mom and dad, and for the way that they raised me, as well as the impact that my grandmother had on all of our relationships.

TABLE OF CONTENTS

LIST OF TABLES……vi

LIST OF FIGURES……vii

1. Introduction……1
   1.1 Statement of Purpose……1
   1.2 Energy Sources and Renewability……1
   1.3 Solar Irradiance……4
   1.4 Semiconducting Materials……6
      1.4.1 The Quantum Mechanics of Electron Transfer……9
      1.4.2 Direct vs. Indirect bandgap Semiconductors……10
      1.4.3 Semiconductor Doping (Intrinsic vs. Extrinsic Semiconductors)……13
      1.4.4 Traps, Recombination and Carrier Lifetime……14
   1.5 Solar Cells……15
      1.5.1 Solar Cell Efficiency……21
      1.5.2 Antireflection Coatings……22
   1.6 Reflection and Antireflection……22
      1.6.1 Selecting a type of ARC……24
   1.7 SiN_x……26
   1.8 Transparent Conductive Oxides (TCOs)……26
      1.8.1 ITO……28
      1.8.2 Why ZnO, and the chosen dopant, Gallium……29
   1.9 Why PLD (The advantages of Pulsed Laser Deposition)……32
   1.10 Low barrier height contact……35
   1.11 The importance of surface passivation……36
2. Experimental Methods and Characterization Techniques……37
   2.1 Target Preparation / Ceramic Processing……38
      2.1.1 Methods for Pellet Pressing……39
      2.1.2 Methods for Pellet Sintering……40
   2.2 Substrate Preparation……41
      2.2.1 Substrate Cleaning……42
      2.2.2 CTLM patterning via Photolithography……42
   2.3 Film Growth by Pulsed Laser Deposition (PLD)……46
   2.4 Annealing……47
   2.5 DC Magnetron Sputtering of Reference Metals……48

2.6 X-ray Diffraction (XRD) 48
2.7 Profilometry 49
2.8 UV-vis spectrometry 49
2.9 Four-point probe and Hall effect measurements 49
2.9.1 Four-point probe 50
2.9.2 Hall effect 51
2.10 Ellipsometry 55
2.11 Two-point probe specific contact resistivity measurements 56
3. Manuscript 61
4. References 84
APPENDIX 91
A.1 Optimization of Dopant Concentration, wt% Ga 92
A.1.1 Structural Characterization by XRD 93
A.1.2 Optical characterization by UV-vis spectroscopy 95
A.1.3 Electrical characterization by Hall effect and 4-point probe 98
A.2 Atomic force microscopy (AFM) of GZO as a function of O_2 pressure 99
A.3 Optimization of Film Thickness 102
A.4 Investigation of Refractive Index 103

LIST OF TABLES

Table 1 Different TCOs used for various types of solar cells, from Fortunato[31] 28
Table 2 Target preparation conditions 41
Table 3. CTLM measurements: measured sheet resistance, expected sheet resistance (from four-point probe technique), transfer length, contact resistivity, and goodness of fit 76

LIST OF FIGURES

Figure 1 A 2008 survey of energy use in the United States [2] 2
Figure 2 Efficiency vs. time for research solar cells [4] 3
Figure 3 ASTM standard reference spectra of solar irradiance[6] 5
Figure 4 Radiation map of the United States[7] 6
Figure 5 Ranges of conductivity for insulators, semiconductors, and metals, along with some material examples [9] 7
Figure 6 Energy band diagram for Si[9] 12
Figure 7 Energy band diagram for ZnO[12] 13
Figure 8 Diagram of a solar cell[15] 16
Figure 9 P-type and n-type semiconductor band diagrams (a) before and (b) after contact 18
Figure 10 semiconductor-semiconductor band diagrams for an n-type emitter and n-type ZnO (a) before and (b) after contact 19
Figure 11 Light that is incident on a two-layer sample causes outgoing, reflected light waves to be completely out of phase. Destructive interference leads to antireflection. 23
Figure 12 Wurtzite crystal structure diagram[40] 31
Figure 13 Comparison of film fabrication processes[43] 35
Figure 14 MicroChem procedure for creating reverse image photoresist patterns[55] 44
Figure 15 Cross-sectional views of the photolithographic process and subsequent metal deposition 45
Figure 16 Schematic of the pulsed laser deposition chamber 47
Figure 17 An example measurement using the van der Pauw configuration[60] 53
Figure 18 Sample TLM wafer as well as graphical relations and equations[63] 57
Figure 19 Sample CTLM wafer as well as graphical relations and equations[65] 58
Figure 20 Mask for CTLM structures on a 2.75 cm x 2.75 cm wafer, and a close-up of one structure, with ring distances indicated 66
Figure 21 Plot of resistance vs. distance for a mesa structure, showing raw resistance data as well as data corrected for the geometry of the circular test structures 68
Figure 22 XRD data for 1 wt.% Ga-doped ZnO deposited onto (100) single crystalline Si substrates, deposited at varying oxygen deposition pressures 70
Figure 23 XRD plots of (a) Undoped ZnO and (b) 1 wt.% Ga-doped ZnO deposited at 5 mTorr O_2 pressure onto (100) Si, shown before and after forming gas annealing. 71
Figure 24 Hall measurement data, featuring resistivity, mobility, and carrier density as a function of oxygen pressure deposition environment 73

Figure 25 UV-vis measurements of transparency as a function of O_2 deposition pressure 74
Figure 26 Reflectance vs. Wavelength data for GZO films varying from 60nm to 225nm on textured, monocrystalline Si solar cells, as well as a solar wafer with no ARC present (naked Si). Also included is a SiNx ARC on the same type of substrate. 78
Figure 27 Current-Voltage measurements for two samples: Black (square marker) data corresponds to cells with sputtered Ag front contacts. Blue (triangle marker) data corresponds to cells with DuPont PV17S screen-printed front contacts. Corresponding efficiency, fill factor, open circuit voltage, and short circuit current are reported for each. (Color available online.) 81
Figure 28 XRD data of GZO pellets with various amounts of Ga dopant 94
Figure 29 Transmission vs. Wavelength of 1 μm thick GZO films of various dopant concentrations. The decline in transmission at the longer wavelengths approaching the IR is not present in thinner films, as will be seen later. 96
Figure 30 Transmission vs. Wavelength for the short wavelength range 97
Figure 31 Resistivity vs. dopant concentration. Measurements were made by 4-point probe and by the Hall effect method. The data points are from 4-point probe measurements, and the error bars correspond to Hall effect measurements. 99
Figure 32 AFM images of 1 wt% Ga-doped ZnO at O_2 deposition pressures of (a) 1 mTorr, (b) 5 mTorr, and (c) 30 mTorr 102
Figure 33 Transmission vs. Wavelength data for GZO films on glass substrates. The GZO films range from 30nm to 200nm in thickness 103
Figure 34 Refractive index and absorption coefficient vs. wavelength of 90nm thick GZO films deposited at 1, 5, and 30 mTorr of oxygen pressure during PLD 104

1. Introduction

1.1 Statement of Purpose

The motivation of this research involves finding efficient, renewable energy via solar cell research. One such aspect of solar cells involves an antireflection coating. It is the purpose of this thesis to explore a particular antireflection coating, which is proposed to replace the current antireflection coatings for its conductive abilities and abundance of raw materials. This thesis will begin by explaining world energy resources, then explain how solar cells operate, and describe the structure of solar cells, and finally explore the optical, electronic, and contact properties of an antireflection coating made of gallium-doped zinc oxide.

1.2 Energy Sources and Renewability

The world today is very dependent on fossil fuels such as coal, oil, and natural gas. Eighty percent of worldwide energy use is made up of fossil fuels [1]. The scarcity of these nonrenewable resources has led to a focus on alternative energy sources, some of which are renewable, and some of which are not. While fossil fuels and nuclear power are fairly efficient energy sources, they require non-renewable resources and have

negative environmental impacts. A survey of the United States' energy resources is shown in the figure below.

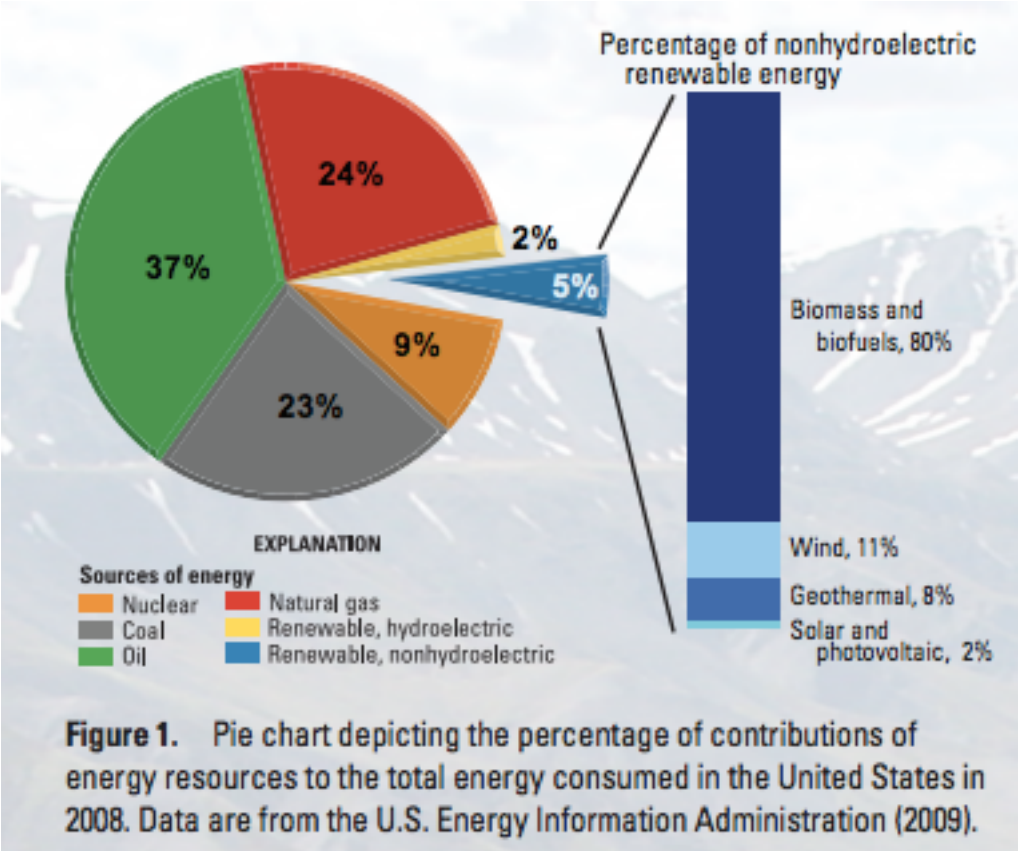

Figure 1. Pie chart depicting the percentage of contributions of energy resources to the total energy consumed in the United States in 2008. Data are from the U.S. Energy Information Administration (2009).

Figure 1 A 2008 survey of energy use in the United States [2]

Some of the renewable energy source options include hydropower, wind power, and solar power. While hydropower requires a vast amount of land over which water can flow, and wind power requires an active, steady wind, solar power faces much smaller, mountable obstacles. Solar (like wind) power requires a storage mechanism, for times when the sun is not shining (or when the wind is not blowing). It also requires

altering the produced DC current into AC current, and will require higher efficiency and lower cost before it is a cost-effective method of energy production. However, these obstacles are mountable, and likely to be overcome[3]. As time progresses, the hope is that solar cell efficiency will increase while price will decrease as Moore's law would predict. The figure below is from NREL and shows a graph of research-cell efficiencies vs. time.

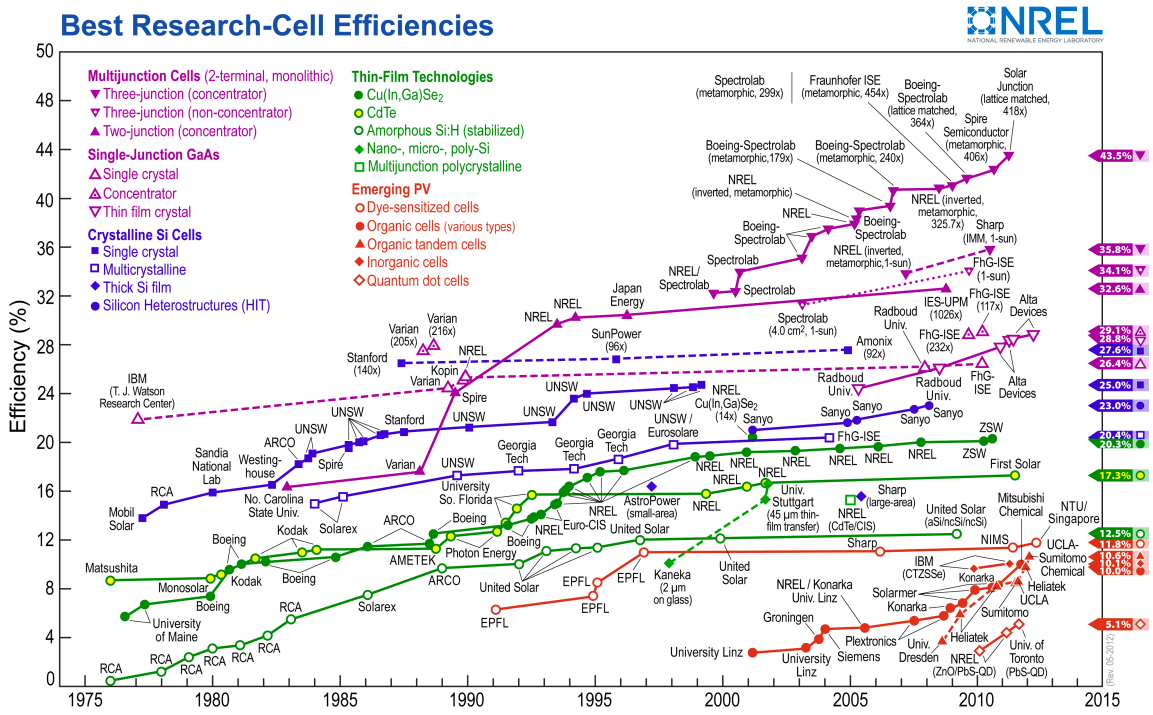

Figure 2 Efficiency vs. time for research solar cells [4]

One such way to increase efficiency in solar cells is to harness as much of the irradiated solar energy as possible. After all, the sun produces enough radiant energy

each day to provide the power needs of the current population for 27 years. Or to think of it another way, the amount of solar radiation that reaches the earth in a span of three days contains the same amount of energy as what is stored in all fossil energy sources.

One such way to better harness the sun's irradiated energy using solar cell technology is to employ a top layer called an antireflection coating. The better this coating at transmitting light into the subsequent solar cell layers (as opposed to absorbing or reflecting it), the more efficient the solar cell. To better understand how to design this coating, it is important to understand what kind of light the sun produces. The next section discusses solar radiation.

1.3 Solar Irradiance

Light consists of photons, which follow properties of both waves and particles, exhibiting the wave-particle duality. Each photon follows the formula $E = \frac{hc}{\lambda}$, where E is energy, h is Planck's constant, c is the speed of light in vacuum, and λ is wavelength[5].

The sun emits photons with a wide range of energies and wavelengths. The ASTM standard for solar irradiance, provided by NREL is shown in Figure 3.

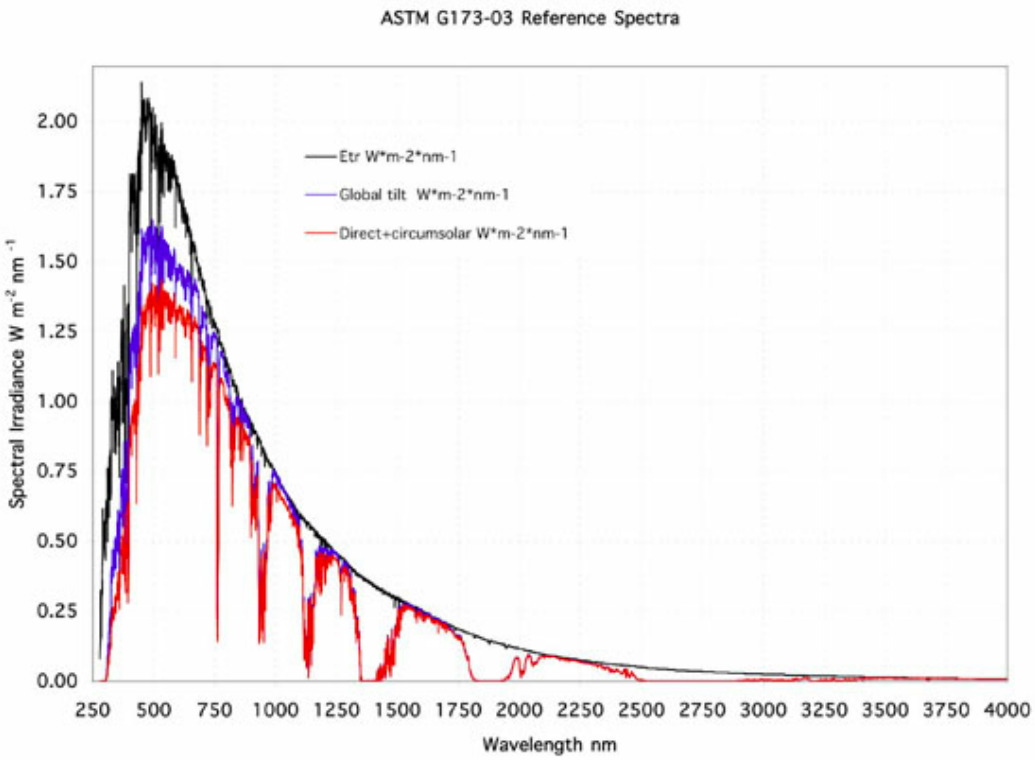

Figure 3 ASTM standard reference spectra of solar irradiance[6]

The standard estimate for terrestrial irradiance is the AM1.5 reference spectrum. The wavelength range and intensities throughout determine in which wavelength ranges one should plan to maximize the antireflection and transmission properties of the ARC. More specifically, the figure below shows how much radiation reaches different areas of the United States.

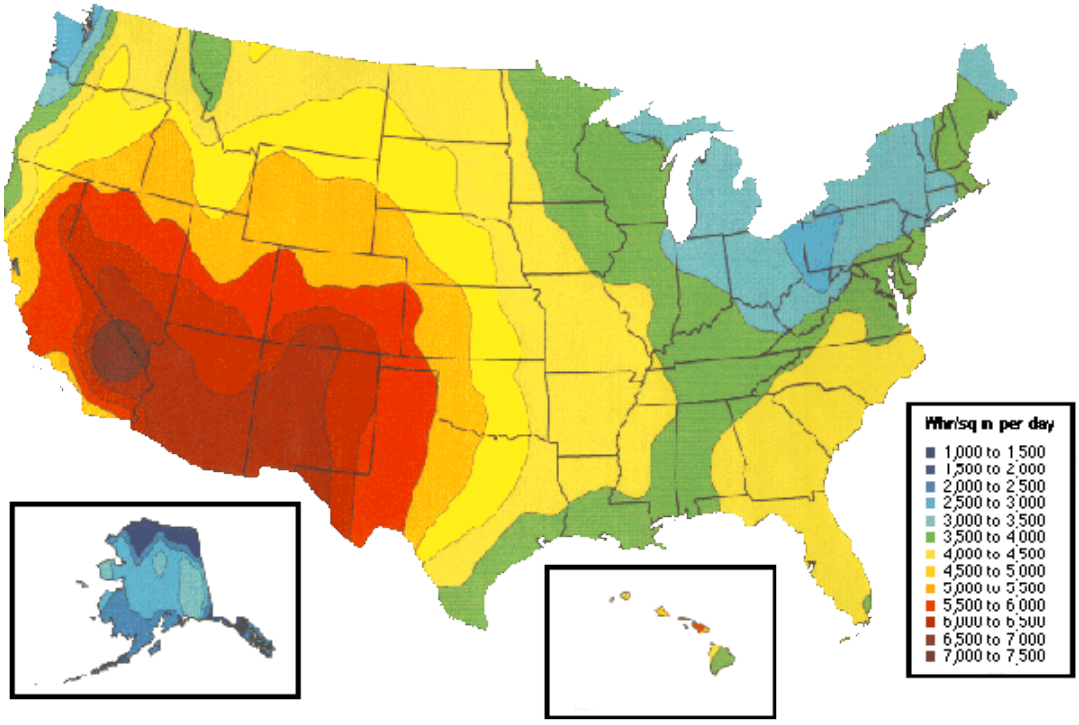

Figure 4 Radiation map of the United States[7]

Through considerations of energy sources and renewability, there is legitimate motivation for finding ways to make solar power efficient, cost-effective, and employed in the United States. This thesis aims to present one way in which solar research can provide a means to enhance this technology.

1.4 Semiconducting Materials

To understand the construction of a solar cell, one must first understand how semiconductors function. There are essentially three types of materials: conductors,

insulators, and semiconductors. Conductors are materials that contain many free electrons, meaning that they are not bound to specific sites and are free to move, thus constituting a current. Insulators do not have mobile electrons and are unable to sustain an electrical current. Semiconductors lie between these two extremes. This section describes this class of material and how they are relevant to solar cell technology. Ohm's law describes the current density relative to the applied electric field, and the current conductivity determines the type of material, be it conducting, semiconducting, or insulating [8].

Current density is described by the formula: $J = \sigma E$, where J is current density (in amperes per square centimeter), E is the applied electric field (in volts per centimeter), and σ is the conductivity of the material (in mhos per centimeter). Conductivity is an easy way to distinguish each type of material. Metals have a conductivity around 10^3 to 10^6 mhos/cm, insulators around10^{-11} to 10^{-8} mhos/cm, and semiconductors around 10^{-7} to 10^4 mhos/cm [8-9]. Figure 5 shows the conductivity ranges of each material type, along with some examples.

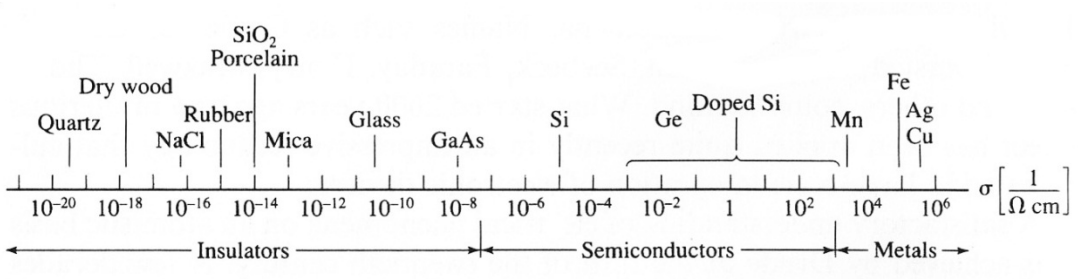

Figure 5 Ranges of conductivity for insulators, semiconductors, and metals, along with some material examples [9].

Unlike conductors or insulators, semiconductors do not have a fixed conductivity. Perhaps the most useful semiconductor property is that electrons, holes, or both can carry the electrical current. This property allows for the development of solar cells, transistors, and integrated circuits [8].

When in a crystalline form, a material is characterized by an ordered array of the atoms that make up the material. These crystalline structures have periodically repeating subsections, which are the unit cells. If sections of crystalline material exist, but each sections exists in independent orientations so that there are discontinuous interfaces, the material is polycrystalline, and if no atomic periodicity exists, the material is amorphous. Semiconductors exist in each of the three forms.

The presence or lack of crystallinity, or atomic structure, affects many properties of a material such as the electrical and optical properties, and thus the performance of the photovoltaic cells made from these semiconducting materials. Thus, it is important to understand crystal structures. An ideal crystal contains regular repetitions of identical structural units, called unit cells. A unit cell can contain just a single atom, or even millions of atoms. Crystal structure of a unit cell describes this periodic structure of discrete points, which is the lattice. Each lattice point contains an atom or group of atoms called the basis. The lattice plus the basis describes the crystal structure. The conventional scheme for defining a crystal plane is to use Miller indices, in which a lattice point is chosen as an origin, intercepts between the plane and the axes are found, and the reciprocals are multiplied to create integers. The result, placed in parentheses,

is the Miller index of a crystal plane[8, 10]. Silicon, for example, can exist as (100), (110), or (111). This describes the crystal plane chosen as the surface of a wafer [8].

1.4.1 The Quantum Mechanics of Electron Transfer

The way in which electrons move through a semiconducting material is important to note, as this translates to how well or poorly the material can conduct electricity. Electrons, as quantum particles, have a periodic potential energy function in an ordered, periodic array of atoms. The wave function follows Schrodinger's equation,

$$\Psi(x) = U(x)\exp(ikx)\exp(-iEt/\hbar)$$

where U(x) is the potential energy, periodic in the crystal case, and wave function $\psi(x)$. Solving the Schrodinger equation yields solutions that, for a periodic potential energy in an infinite lattice, follow the Bloch wave function,

$$\psi_{nk(r)} = \exp(ik\cdot r)u_{nk}(r)$$

stating that the periodic Bloch function has the same periodicity as the potential, u[11].

Energy versus momentum (E vs. k) plots reveal that only certain energies are allowed for electrons in the crystal, via corresponding allowed energy bands. The differences in energies between the highest point in the lower set of allowed bands and the lowest point on the higher set of allowed bands reveal the band gap.

At 0 Kelvin, the highest completely filled band is called the valence band, and the lowest unfilled energy band is called the conduction band. These bands can be used to classify the conductors, insulators, and semiconductors described before. If the

conduction and valence bands overlap, the material is a conductor. If the bands have a large separation, the material is insulating. If the bands are separated but relatively close, the material is semiconducting. In the cases where a separation is present between the bands, the gap is called the band gap, is denoted by E_g, and is measured in electron-volts (eV). In this gap, there are no allowed energy states for electrons to occupy. In all cases, when a band is full, it is unable to conduct a current. This is true because a current-carrier such as an electron must accelerate, which involves a change in energy, which requires changing location on the energy-momentum diagram, but in a full band, the other locations are already occupied by other electrons, and the Pauli Exclusion principle states that no two electrons in a given crystal may have identical quantum numbers; that is, they may not occupy the same energy-momentum position. This explains why materials with only full bands are insulating.

As temperatures increase from 0 K, some electrons will gain enough thermal energy to make it into the conduction band, allowing these electrons to participate in current flow. By moving into the conduction band, the electron leaves a hole in the valence band, rendering it no longer full, and thus capable of carrying current [8].

1.4.2 Direct vs. Indirect bandgap Semiconductors

Moving further in the understanding of semiconductors, it is important to understand the difference between direct and indirect bandgap semicondcutors. A look at two energy vs. momentum diagrams, or band diagrams, in Figure 6 and Figure 7

show that, sometimes, the difference between the highest point on the valence band and the lowest point on the conduction band occurs at the same k (momentum) value (direct bandgap semiconductors), requiring only a change in energy for an electron to jump from the valence to the conduction band. For other types of semiconductors, the valence band maximum and conduction band minimum occur at different k values (indirect bandgap semiconductors), and thus an electron must change not only energy, but also momentum in order to be excited into the conduction band. This generally involves thermal excitation, and is a limitation of indirect bandgap semiconductor solar cells compared to direct, due to the necessary heating of the cell and results in poor efficiency. Also, additional heat is present as a result of higher-energy photons creating deeper electron-hole pairs in the bands, of which the holes and electrons move to the band edges and give up extra energy as heat to the lattice.

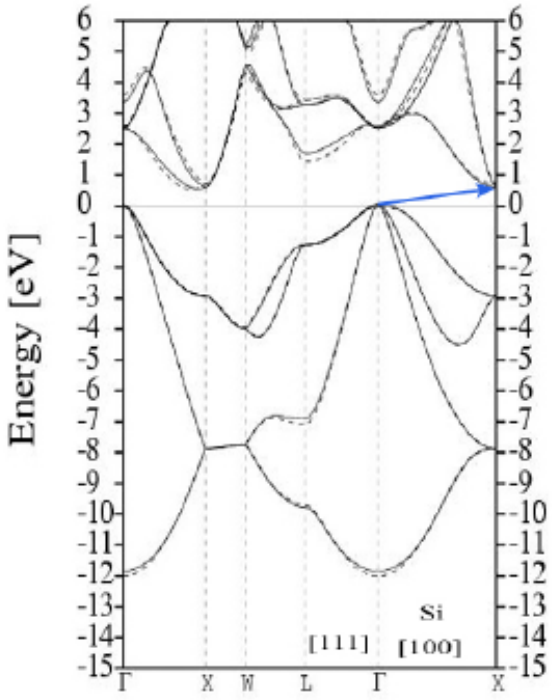

Figure 6 Energy band diagram for Si[9]

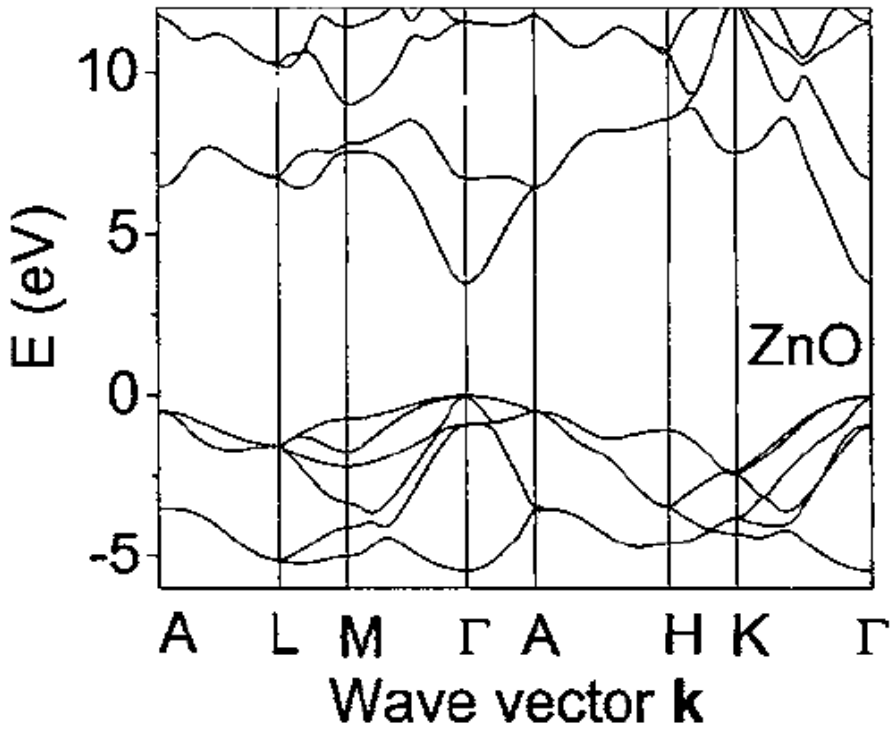

Figure 7 Energy band diagram for ZnO[12]

1.4.3 Semiconductor Doping (Intrinsic vs. Extrinsic Semiconductors)

Semiconductors can be of a pure material form, or they may contain impurities. This section will discuss the difference between intrinsic and extrinsic semiconductors, and the effects of doping.

Intrinsic semiconductors are defined as having the same number of electrons in the conduction band as holes in the valence band. Conductivity is determined by the number of electrons, the number of holes, and the mobility of the current carriers. To increase the conductivity of a sample, one may choose to add a dopant (a type of

impurity) such that the material is provided with extra holes or electrons. By doping the material, it is made extrinsic, which influences the type and amount of charge carrier and conductivity of the semiconductor. Extra electrons means the impurity is a donor. Extra holes means the impurity is an acceptor. These impurity atoms often replace host semiconductor atoms on their crystal lattice sites. For example, in gallium-doped zinc oxide, the gallium atom will replace the zinc atom, and the extra electron from the gallium is only loosely attached, and easily donated (for example, with energy from heat). The detached electron is able to move freely and populate the conduction band, where it can carry a current [8-9].

At low temperatures, electrons are scattered by impurity atoms and lattice defects. As temperatures increase, the mobility of current carriers is reduced, due to lattice vibrations. At room temperature, more electrons are excited into the conduction band, increasing the number of current carriers, and thus providing a purpose to dope[9].

1.4.4 Traps, Recombination and Carrier Lifetime

When considering the interaction of light with semiconductors, it is important to understand how and when light stimulates electrons from the valence band to the conduction band, creating electron-hole pairs. Light of sufficiently short wavelengths can stimulate this behavior, however, some of the electron-hole pairs will recombine within the semiconductor. A semiconductor has some density of traps[13], which are defects that facilitate electron-hole recombination[8]. The rate at which electron-hole

pairs recombine is described and analyzed by lifetime measurements. Recombination lifetime, or carrier lifetime, is defined as the time it takes a system to return to thermal equilibrium after an incident pulse of light[14]. The longer the lifetime, the more effective a solar cell at preventing recombination and preserving the optically generated electron-hole pairs.

Recombination rates are proportional to electron or hole concentrations, so for high optical concentration levels, the generated carrier density affects recombination rate. The lifetime, which measures the time available to collect the optically generated carriers, increases until a saturation point of high carrier concentrations, which increases photocurrent[8].

1.5 Solar Cells

The purpose of a solar cell is to convert energy form the sun into electrical energy and to deliver this energy to an external load. Now that semiconductor interactions and solar irradiation are well-known, these materials and resources can be used to describe the concept of solar cells.

Solar cells are comprised of a few basic layers. From the bottom up, there is traditionally a back contact, generally of aluminum, followed by a bulk semiconducting layer which is usually p-type, and then a thinner, highly doped n-emitter. On top of this is a transparent conducting layer, followed by an antireflective layer, and finally, top

contacts, generally silver. In some cases, the conducting layer and the antireflective layer are one in the same.

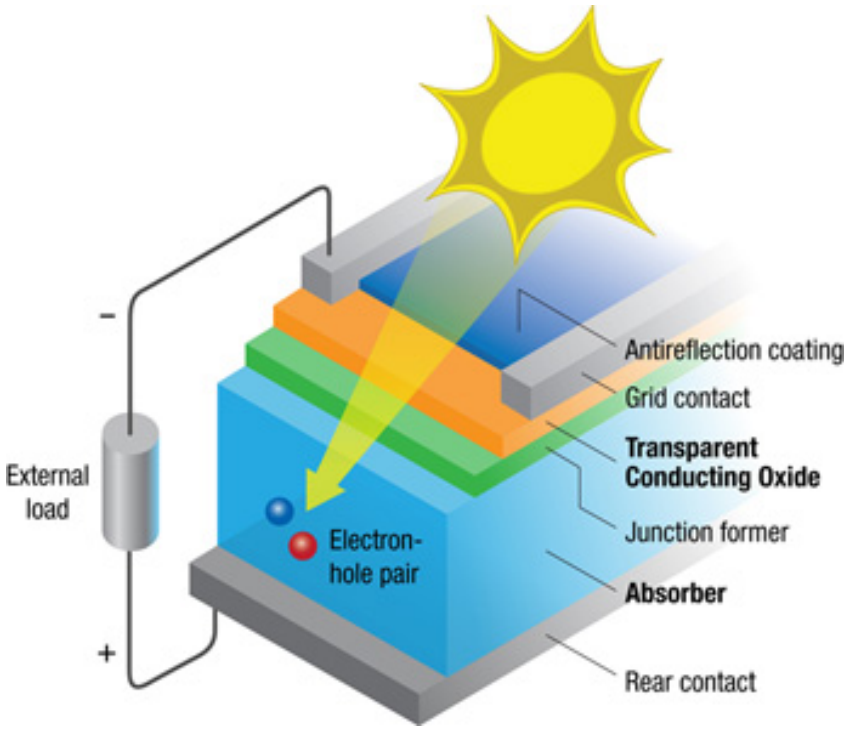

Figure 8 Diagram of a solar cell[15]

When photons from the sun are incident on the cell, if they have a sufficient amount of energy, they knock off one electron from the semiconductor, leaving a hole. With an external path provided by the contacts, these electrons flow, constituting a current. The metal contacts facilitate the flow of this current, but it is the bulk p-type and n-emitter junction, referred to as the p-n junction, that creates the driving force.

When p-type and n-type semiconductors are joined together, the transfer of electrons and holes takes place at their junction. The high concentration of holes in the p-type material and the high concentration of electrons in the n-type material cause a concentration gradient across the junction. Free electrons diffuse along the gradient and combine with holes to form negative ions at the acceptor impurity sites, and positive ions are left behind in the n-region at donor impurity sites

After some time, however, the buildup of holes and electrons near the junction forms a barrier to resist further transfer, which makes it difficult for electrons to move from the n-type into the p-type silicon. These fixed charges constitute an electric field and repel carriers that are of like charge. The building field discourages any further diffusion across the interface, and when equilibrium is reached, there is a space charge volume called the depletion region, caused by the depletion of free carriers.

The band diagram of p-type and n-type material before and after contact is shown in the figure below. When contacted, the bands shift and bend the depletion region to align the Fermi level across the junction. This p-n junction (which is a type of diode) is the most basic form of a semiconductor device.

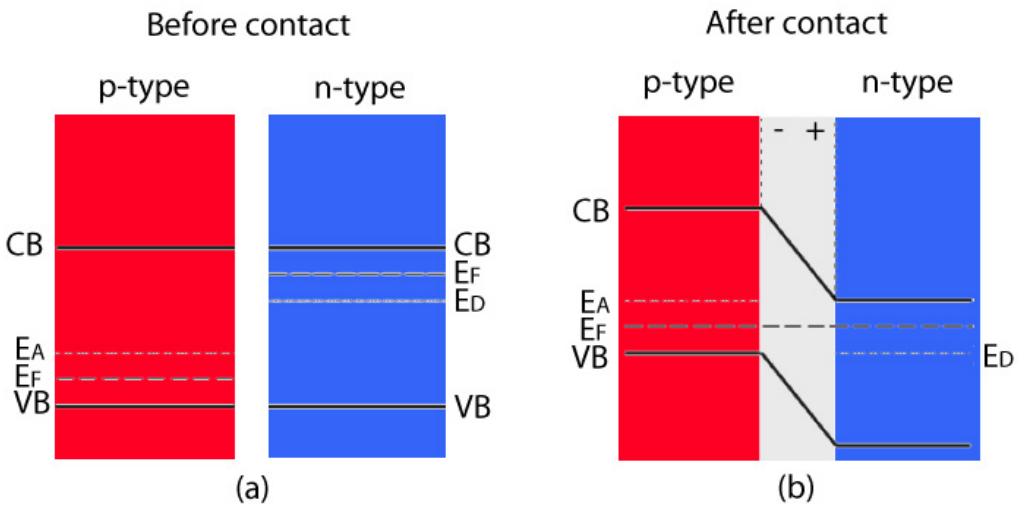

Figure 9 P-type and n-type semiconductor band diagrams (a) before and (b) after contact

For a solar cell, incoming light (photons) collides with valence band electrons, boosts them into the conduction band, and leaves behind holes, creating an electron-hole pair. This junction's electric field, which separates electron-hole pairs when incoming photons interact with the semiconductor, makes it possible to collect individual holes and electrons. The electrons are collected in the n-type semiconductor, and the holes in the p-type. Thus, there is a forward bias when light shines on the cell[8].

The structure of a solar cell is such that above the stacked p-n junction, there sits an antireflective coating. When choosing an ARC, it is preferable to maintain n-type to n-type (or p-type to p-type contact, but for the purposes of this thesis, focus will be placed on n-to-n contact). The semiconductor-semiconductor interaction possibilities for an n-type emitter and n-type ZnO are shown in Figure 10. This example is representative of n-to-n type contacts, but the specific example is relevant to this thesis.

The theoretical work function of this configuration is 0.2 eV and has been experimentally measured to be 0.4 eV[16]. It is of note that ZnO is inherently n-type, and thus p-type doping is more difficult, however possible.

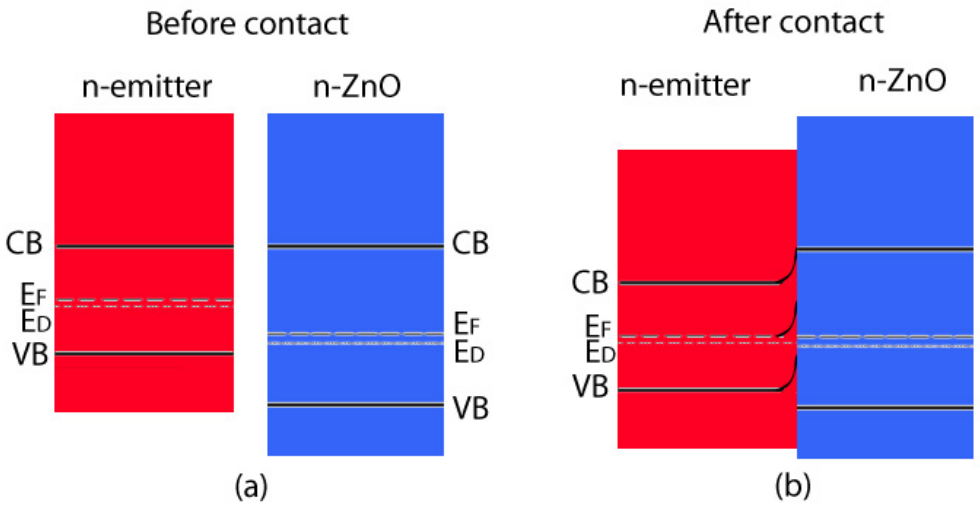

Figure 10 semiconductor-semiconductor band diagrams for an n-type emitter and n-type ZnO (a) before and (b) after contact

Shown are the locations of the Fermi levels, the energy levels of the electrons, the conduction band minima, and the valence band maxima. When brought into contact, the materials are made into a single semiconductor crystal. The Fermi levels align, and the figure shows the energy vs. displacement diagram in thermal equilibrium. It is shown that alignment of the Fermi levels requires band bending on the side of the emitter.

When incoming light (photons of various wavelengths) is incident on a semiconductor, a fraction of the photons that strike the surface are reflected and the

remaining photons enter the semiconductor, either to be absorbed within or to be transmitted through. Most of the photons that are absorbed are what give rise to the necessary electron-hole pairs, which are the source of photocurrent and thus photovoltage. The antireflective coating is included to reduce these losses due to reflection. With fewer losses, more photons are available to knock off the electrons that constitute the current flow[8]. The main focus of this thesis is optimizing and implementing a particular antireflection coating. In addition, reflection losses can be reduced in the case of a single-crystalline material by using anisotropic etching to make pyramid-type texturing[17].

When designing a solar cell, a consideration of the electrical and optical properties is important in order to optimize the cell's performance. Front contacts should cover as small an area as possible so as to maximize the number of incident photons on the face of the cell. Contact fingers should be spaced within the carrier diffusion length, and be thin enough to avoid blocking incident photons, meanwhile not so thin that the series resistance is increased. Also, contact fingers require that the top semiconductor layer (in our case n-type) be heavily doped to assist conduction, but not so high that the diffusion length is diminished. This allows the underlying p-type layer to be lightly doped so that carrier collection is maximized while open circuit voltage is not sacrificed. The difference between the highly doped top n-region and the lightly doped bottom p-region means that the depletion region lies more in the p-type layer,

and that the junction occurs near to the surface. This decreases the probability of recombination before the charge carriers can be collected.

1.5.1 Solar Cell Efficiency

Solar cell efficiency is dependent on reflectance efficiency, thermodynamic efficiency, charge carrier separation efficiency, and conductive efficiency. One key factor in evaluating the performance of a cell is fill factor, which is the ratio of the actual maximum obtainable power to the product of the open circuit voltage and short circuit current[18]. Typical commercial cells have a fill factor of greater than 0.7, while grade B cells have fill factors between 0.4 and 0.7[19]. The higher the fill factor, the less current is dissipated and lost internally. Single p-n junctions in crystalline silicon devices have a theoretical limiting power efficiency of 33.7%, defined by the Shockley-Queisser limit, defined in 1961[20]. Modern commercial mono-crystalline solar cells can reach approximately 22% conversion efficiency, the losses from practical concerns such as reflection and blocked light from the surface contacts. For a theoretical cell with an infinite number of layers and a concentrated sunlight source, the maximum efficiency limit reaches 86%[21].

1.5.2 Antireflection Coatings

Anti-reflective coatings, once a German military secret[22] and later patented by Katharine Blodgett in 1938[23], are now an integral part of many devices. The goal may be to achieve anti-glare properties on lenses, or to capture as much energy as possible in a solar cell, among other uses. This section discusses what antireflection is, strategies to achieving anti-reflective coatings, categories of ARCs, fabrication techniques, and materials used to create the most efficient ARCs possible while maintaining durability and minimal cost.

1.6 Reflection and Antireflection

Reflectivity is a property that relates the incoming and outgoing wavelengths of a beam of light as it travels through one medium and into another. Reflection occurs when light travels through a medium and reaches a transition to another medium. The refractive index (n) quantifies the speed of light in a medium with respect to light in vacuum. The traveling light reaches a medium with a different index from its own, and light is either reflected, or transmitted (at which point it can be absorbed, scattered, etc.). If the reflected waves are completely out of phase, which occurs when the film is an odd multiple of a quarter wavelength of the incident light, then reflected waves will undergo destructive interference, canceling each other, and resulting in no reflection as

shown in Figure 11. The Fresnel equation offers a mathematical model to relate reflectance to the indices of refraction, given in Equation 1[24].

At normal incidence,

$$reflectance = \left[\frac{n_{air}n_{substrate} - n_{film}^2}{n_{air}n_{substrate} + n_{film}^2}\right]^2 \quad \text{Equation 1}$$

For r=0,

$$n_{film} = \sqrt{n_{air}n_{substrate}}$$

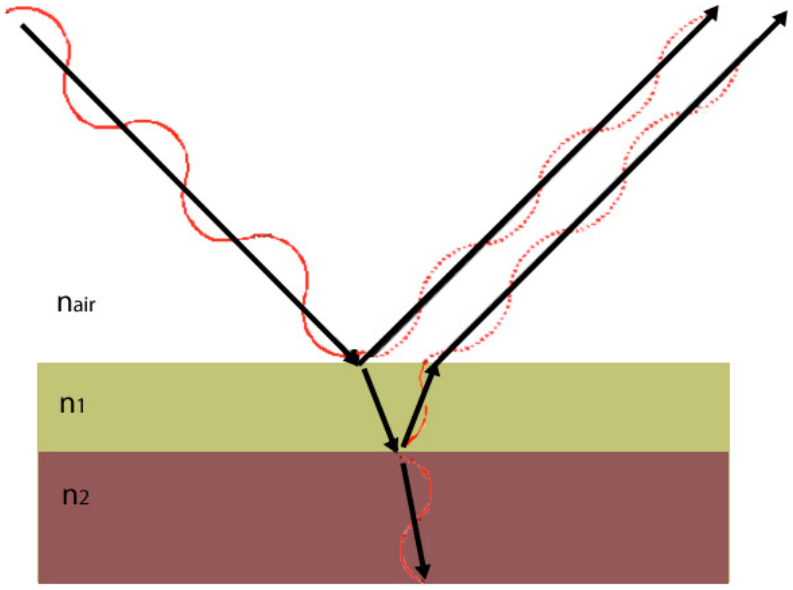

Figure 11 Light that is incident on a two-layer sample causes outgoing, reflected light waves to be completely out of phase. Destructive interference leads to antireflection.

In materials, reflection effects change depending on the relevant refractive indices, polarization of light, lattice constants, and film thicknesses. In addition, it is important to keep the application in mind, as it is often important to have anti-reflection over, say, a wavelength range, or in all directions, or to be insensitive to polarization.

1.6.1 Selecting a type of ARC

The selection of material for an ARC involves consideration of the available materials and the underlying material properties, as well as the application. There are several materials with the proper refractive index for ARC applications, the range being between 1.4 and 2.7 These include SiO, SiO_2, Si_3N_x, Si_3N_4, Al_2O_3, Ta_2O_5, TiO_2, polymers, gallium, carbon, and organics[25].

Some practical concerns also exist when choosing an ARC. The ARC must not damage the semiconductor, which could cause the surface recombination velocity to increase and the magnitude of the photocurrent to decrease. The ARC must also consider the broad range of optical wavelengths present from the sun; materials that can capture the broadest wavelength range between 200 nm and 1300 nm should be considered. The ARC must also withstand being exposed to air and direct sunlight for long periods of time.

There are many categories of anti-reflective coating, such as homogeneous and inhomogeneous ARCs, single, double, multi-layer, or gradient refractive index (GRIN)

ARCs, and ARCs based on surface topography, such as porous ARCs and biomimetic photonic nanostructures such as "moth's eye."[26] Single layer ARCs are generally good at moderately suppressing reflectance to ~2.5% for a very broad spectral range (450-1100nm) at normal incidence. Gradient refractive index (GRIN) ARCs have a variety of refractive index profile curves, which can be linear, parabolic, cubic, quintic, exponential, etc., and comply with the Rayleigh effect. GRIN profiles give very low percentages of reflectance. The underperformance arises from the difference in refractive index (n) between the ARC and air, and also from the difference in the absorbing substrate, which has a complex n, and the transparent ARC with real n, causing a mismatch. This violates the Rayleigh effect[26]. There are also ARCs which are biomimetic photonic nanostructures, or "moth's eye" structures. They are imitated corneal surfaces with a hexagonal array of sub wavelength conical or cylindrical nanostructures of 100nm diameter and 170nm spacing. The first structures of this type were produced using three lithography gratings[27]. Using materials like GaSb on quartz and fused silica substrates reduces reflectance to 0.5% in the 400-800nm wavelength range[28].

The scope of this research would not greatly benefit from a GRIN ARC, as the single layer coating is so thin, the graded effect would not have a large effect. Additionally, it is important that our ARC is transparent, and thus the porous and biomimetic structures would not be ideal for solar cell applications.

1.7 SiN_x

Silicon nitride (SiN_x) is a commonly used class of materials for ARC applications. The nitride must be low-absorbing, serve as a barrier layer to control metallization, and promote electronic processes that can passivate the surface and the bulk of the device to optimize optical and electronic properties of the cell. Its use is common in the device industry because SiN_x is mechanically strong, has good dielectric properties, and provides an excellent barrier against moisture corrosion and mobile ions[29]. The Si content in the SiN_x can tune the refractive index to be from 1.9 to 2.4[30]. This ARC, which is an insulator rather than a conductor, requires a fire-through process of the silver contacts that are printed on top of the solar cell to obtain ohmic contact. There has been much interest in moving from insulating ARCs such as SiN_x and into a conductive ARC realm.

1.8 Transparent Conductive Oxides (TCOs)

Transparent conductive oxides (TCOs) are materials which are just that—optically transparent and electrically conductive. The conductive nature of TCOs allows them to act as electrode elements as well as antireflective coatings on solar cells, rending them more efficient than cells without these improved junction characteristics. Photovoltaic devices require that at least one of the electrodes provide optical access as well as a low resistance electrical contact. Materials that are both transparent and

conductive occur in very thin, pure metals, highly doped, conjugated, organic polymers, and degenerately doped, wide-bandgap oxide or nitride semiconductors. The performance of TCOs is directly related to the band structure of the material, although in some cases, amorphous materials perform just as well.

Baedeker reported the first TCO in 1907, using a primitive vapor deposition technique to deposit a thin film of cadmium oxide (CdO). Since then, TCOs have become commercially relevant, including materials such as indium oxide, tin oxide, and zinc oxide. Some of the TCOs in use for a variety of cell types are outlined in Table 1.

In the case of oxides, which are generally insulating in the undoped state, require degenerative doping to increase the free carrier density and move the Fermi level into the conduction band. Point defects such as oxygen vacancies or the addition of impurities are common sources of electron donors. The added impurities find substitutional sites in the lattice, as is the case with Al-doped ZnO, Sn-doped In_2O_3, and Sb-doped SnO_2. It is important to note, however, that too high of an impurity level will cause a decrease in carrier mobility—a tradeoff when optimizing resistivity[31]. The following sections will cover indium tin oxide (ITO), a common TCO, as well as doped ZnO, a TCO that is a proposed replacement of ITO due to the abundance of the materials in comparison with ITO, and thus the relative cost benefit.

Table 1 Different TCOs used for various types of solar cells, from Fortunato[31]

Cell Type	TCO in Current Use	TCO Needs	Materials Goals
Heterojunction with intrinsic thin layer (HIT) cell	Indium tin oxide (ITO)	Smooth, good interfacial properties, very good conductivity, low temperature deposition, light trapping	Indium zinc oxide (IZO), indium free materials, ZnO
Copper indium gallium selenide (CIGS)	Intrinsic ZnO/Al:ZnO	Interfacial stability to CdS, low temperature deposition, resistance to diffusion and shorting, need to make/improve the junction	Single layer TCO to replace two layers and CdS layer
CdTe	(SnO_2) Zn_2SnO_4/Cd_2SnO_4	Stable interface to CdS/CdTe at temperature, diffusion barrier	Doping of ZnSnOx materials, single layer TCO
Nano hybrid polymer cell	ZnO, SnO_2, TiO_2	Nanostructure with right length scale, work function matching, interface with organic, correct doping level for carrier transport	Self organized structures core–shell structures, new nonconventional TCOs
Grätzel cell	TiO_2	Nanostructure with high electron mobility	Improved TiO_2 morphology and possible use of doped materials, new non TiO_2 materials
Amorphous Si	SnO_2, ITO, and ZnO; many cells employ two TCOs	Temperature stability, chemical stability, and appropriate texture for both TCO layers	Higher conductivity, texture, and ohmic contact for both TCO layers

1.8.1 ITO

Tin-doped indium oxide, or indium tin oxide (ITO) is a material that, in thin film form, reflects infrared light while allowing visible and ultraviolet light to pass through. This oxide coating is commonly used as an anti-reflection coating for solar collector panels, photovoltaic cells, and windows. While uncoated glass has a refractive index around 1.52, ITO-coated glass has a refractive index of 2.0. Transmittance values can

reach 90%, while typical reflectance measurements are from 8 to 25%[32]. A typical resistivity measurement is 10^{-4} Ohm-cm, though resistivities as low as $8x10^{-5}$ Ohm-cm have been reached[17]. While the reflective and conductive properties of ITO are quite attractive, the cost of these materials is high, as indium is rare.

1.8.2 Why ZnO, and the chosen dopant, Gallium

Before explaining why the choice was made to dope zinc oxide with gallium, I will first explain why zinc oxide was chosen as the base material.

Zinc oxide is an attractive material for its many applications, like transparent conductive contacts, laser diodes, and anti-reflective coatings for solar cells. It is abundant in raw material form, making it much less expensive than indium tin oxide, whose indium constituent contributes greatly to the price. ZnO has another advantage over ITO, which is that it can tolerate reducing atmospheres[33]. ZnO is highly transparent in the visible region, and extremely easy to crystallize. It is easily fabricated using methods such as sol-gel processing[34], chemical vapor deposition[35], DC magnetron sputtering[36], and pulsed laser deposition[37] among others[38]. Using PLD, even at low deposition temperatures, ZnO grows with perfect (0001) fiber texture.

ZnO is an inorganic compound that is a wide band gap semiconductor. The native doping is n-type. Without intentional doping, ZnO has a direct band gap of 3.37 eV at room temperature and a large exciton binding energy of 60 meV[39]. To decrease the band gap, we must alter the undoped ZnO in some way. ZnO is easy to modify by

creating intrinsic defects, like oxygen vacancies or zinc interstitials, or introducing extrinsic dopants.

In the undoped state, ZnO is very resistive. Unlike indium-based materials, the point defects that are native in ZnO are not conducive charge carrier donors. In order to decrease the band gap of ZnO from its undoped energy of 3.37eV, we add substitutional dopant atoms that have one electron more than Zn atoms, so that the dopant atoms may substitute for zinc sites, leaving the extra electron free to move about and act as charge carriers, contributing to conduction. Atoms that have this one extra electron belong to the group IIIA on the periodic table of elements. By doping ZnO with a group IIIA element, the semiconducting material becomes strongly n-type[31].

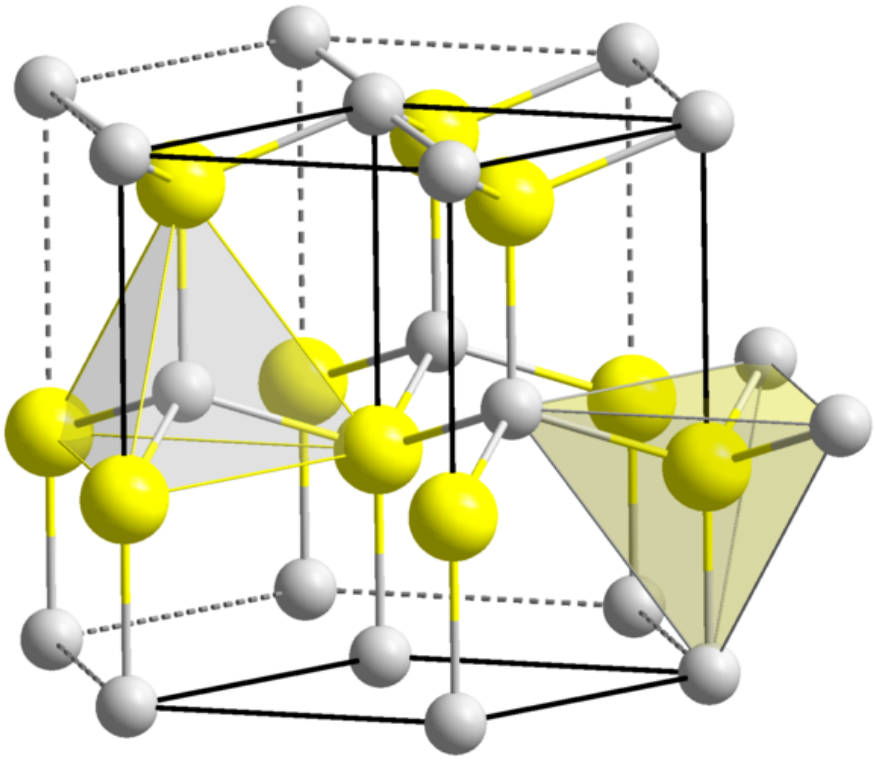

Figure 12 Wurtzite crystal structure diagram[40]

Substitutional doping can be achieved well with dopants such as Al, In, or Ga. Much focus was placed initially on Al doping[41], however, using Al required very precise control of the oxygen present during deposition, as Al is very reactive with oxygen. Gallium was chosen as the dopant for many reasons. Its abundance makes it cheaper than In, and its atomic size matches that of Zn better than Al, causing less lattice distortion and thus less stress in the crystal lattice[31]. As gallium is added to the undoped ZnO, electrical properties improve until a critical point, at which further doping

decreases the conductivity of the material, as there are no longer zinc substitutions to be made or interstitials to be filled, and the excess gallium is a detriment, causing the introduction of a second phase, the spinel Ga_2O_3, whose band gap is larger than that of ZnO.

Ga-doped ZnO provides greater than 90% transmission in the visible range, and has resistivity values on the order of 10^{-5} Ohm-cm[37e].

1.9 Why PLD (The advantages of Pulsed Laser Deposition)

It is possible to form a thin film layer of a metal oxide through many fabrication techniques. ZnO can be deposited via physical vapor deposition techniques such as molecular beam epitaxy, sputtering, vacuum evaporation, ion plating, and pulsed laser deposition, among other methods. In this section, I will explain the many advantages and the few disadvantages of using pulsed laser deposition.

Pulsed laser deposition is versatile. Since the technique's first use by Smith and Turner in 1965, PLD has been used to prepare semiconductor and dielectric films. The technique stemmed the work of Dijkkamp et. al who used PLD to develop high-temperature superconductors in 1987[42]. Since the energy source, unlike many other physical vapor deposition techniques, is outside of the deposition chamber, PLD allows for many new degrees of freedom. One of these degrees is the deposition environment. For Magnetron sputtering, a noble gas (or inert gas), like Argon, is required. However,

PLD may be performed under ultrahigh vacuum, ambient conditions, or in a chosen gaseous environment at a particular pressure.

Additionally, PLD has the convenient stoichiometric transfer of target material to substrate, meaning that the stoichiometry of the target very closely constitutes the stoichiometry of the ablated film. This allows for multicomponent targets and more complex systems. Stoichiometry transfer is difficult with evaporation or magnetron sputtering without using multiple targets. In general, the partial vapor pressures and sputtering products are not the same, causing different concentrations of the thin film grown. The stoichiometry transfer in PLD is due to the fast, strong heating of the target by the intense laser beam. This ensures that all the target components, without regard for their partial binding energies, evaporate at the same time. With a sufficiently high ablation rate, a Knudsen layer forms, is further heated, and forms a high-temperature plasma which then adiabatically expands perpendicular to the target surface. So the material transfer from the target to the substrate happens without much separation of the target components, and collisions between atoms are few. Also, since the spot size of the laser beam is small, these targets can also be small – an additional perk of PLD that many other techniques do not have the luxury of claiming.

The versatility of PLD extends into the laser's degrees of freedom. Many experimental parameters can be changed, such as laser fluence, wavelength, pulse duration, and repetition rate. Each of these can have an influence on film properties.

Preparation conditions can also be altered, like target-to-substrate distance, substrate temperature, and background gas and pressure[42].

There is, however, one main disadvantage of PLD, which is that it covers a small area, with limited uniformity. Though it is an impractical deposition method for large-scale, commercial grade production, it is an excellent research tool, and presents results which are easily transferred to other, larger scale production possibilities.

So, by pulsed laser deposition, ZnO can grow and crystallize extremely easily, even under low energy and temperature deposition conditions. These advantages make PLD the best choice for deposition technique. Uniformity and deposition rates are comparable to other deposition techniques.

A comparison to other film fabrication processes' film quality and capital cost is shown in Figure 13.

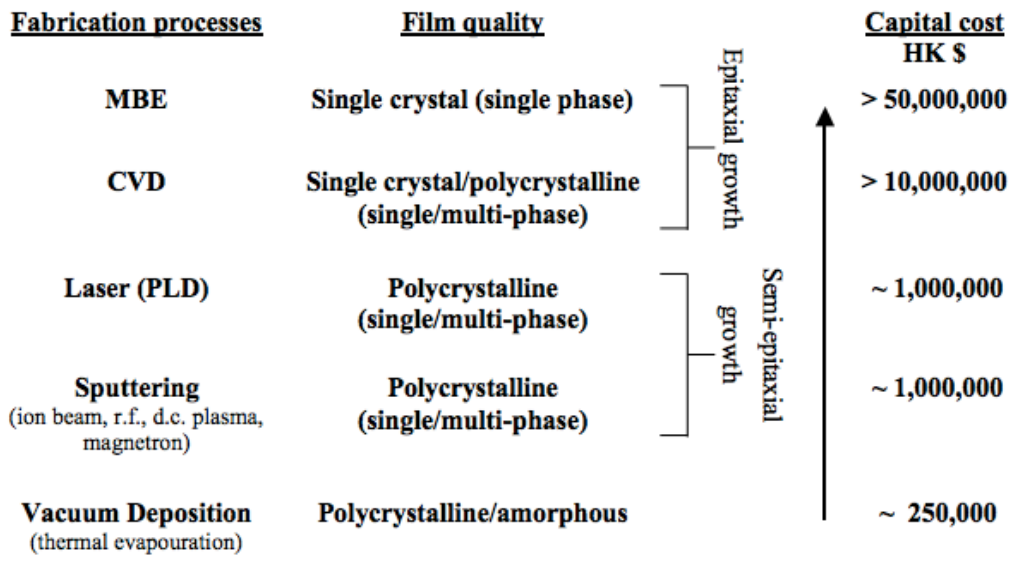

Figure 13 Comparison of film fabrication processes[43]

1.10 Low barrier height contact

Realizing good, ohmic contact is an important parameter to obtain efficient semiconductor devices. An ideal ohmic contact to a semiconductor has no barrier to the flow of charge carriers in the positive or negative direction. When the work functions of the semiconductor and metal are nearly the same and there are no appreciable interface states to pin the Fermi level, an ohmic contact is possible[44]. This creates a low barrier height contact, which is desirable so that conduction electrons can flow freely across the interface. At a constant temperature, a highly doped semiconductor material is essential to the formation of an ohmic contact. A device's performance is often

dependent upon the contact resistance on a highly doped substrate, as is the case for highly doped emitters on solar cells[45]. Good ohmic contact can be achieved when the contact resistance is much less than the total on-resistance of the device. Satisfying this condition results in a negligible voltage drop across the contact, which is necessary to obtain high efficiency in a device[46].

Substrate doping level is of great importance to the achievement of an ohmic contact, as is the selection of the metal with which to create the contact. This thesis will explore the dependence of both in the presence of a GZO ARC[47].

1.11 The importance of surface passivation

The properties of an ohmic contact can strongly depend on the surface of a given substrate. A native oxide layer or the presence of contaminants could cause a reduction in metal adhesion at the metal-semiconductor interface, affecting barrier height and increasing specific contact resistance[48]. This would create electrically active defects that can change the conduction of carriers through the contact. Thus, cleaning procedures and knowledge of passivating layers is of great importance in the fabrication of device contacts. A reproducible semiconductor cleaning procedure that removes contaminants as well as any native oxide layer is necessary prior to performing metallization of a contact[46]. Specifically, any silicon stored in air will form a native SiO_2 layer, which is insulating. To make good contact, we must remove this passivating layer so that the

deposited metal oxide may contact the semiconductor directly and satisfy the dangling bonds. A hydrofluoric acid (HF) dip prior to metallization is a good way to remove this SiO_2 layer.

In addition, annealing in a reducing environment, namely forming gas, is a method of introducing hydrogen H+ atoms to the silicon emitter surface, which is known to improve lifetime[49].

2. Experimental Methods and Characterization Techniques

The creation of gallium-doped zinc oxide (GZO) thin film samples prepared by pulsed laser deposition (PLD) is comprised of a few basic steps. The material must begin as a ceramic pellet and ultimately become a thin film on a chosen substrate. In order to obtain optimal characteristics, substrates must be properly treated before deposition. Patterning is required for samples for which specific contact resistivity measurements are made. For these samples, photolithographic processes are employed to create the desired deposition windows for convenient measurement techniques. Once target pellets and substrates are prepared, a pulsed laser ablates the ceramic, which, under reduced atmospheric pressures, creates a plasma plume. This plume reaches the desired substrate, and a thin film is formed. In some cases, electronic or optical properties benefit from particular annealing processes[50]. The first four sections of this chapter describe the four basic experimental steps necessary to obtain thin film

samples by PLD, namely (1) target preparation / ceramic processing, (2) substrate preparation, (3) ablation, and (4) annealing.

In regards to making intimate contact between film and substrate, reference metals were investigated. The procedure for depositing the assorted reference metals involves DC magnetron sputtering onto prepared substrates. The next section of this chapter describes the methods for sputtering these metals.

The films are characterized to optimize optical and electronic properties to suit conductive, transparent antireflection coating applications. The structural characterization of the films was done by x-ray diffraction (XRD) and profilometry. Optical properties of the films were characterized by UV-vis spectrometry. Electrical properties of the films were characterized by four-point probe resistivity measurements, Hall effect measurements, and two-point probe specific contact resistivity measurements. Refractive index was characterized via ellipsometry. The latter portion of this chapter describes each characterization method employed.

2.1 Target Preparation / Ceramic Processing

Creating a target best suited for PLD of GZO involves pressing a ceramic pellet from an appropriate composition of metal oxide powders, followed by sintering to attain a sufficiently dense pellet. For this work, zinc oxide powder (Alfa Aesar, 99.9%

purity) has been doped with 0-8 wt% gallium oxide (Acros Organics, 99.99+% purity) to examine electrical and optical properties as a function of dopant concentration.

2.1.1 Methods for Pellet Pressing

It is important to be sure that the gallium oxide powder is uniformly mixed into the zinc oxide powder before pressing a pellet. To ensure optimal mixing, the powders are poured into a Nalgene bottle with ball mill media and isopropyl alcohol (IPA). The mixture is ball milled for 8 hours and subsequently poured into a Pyrex dish and set on an 80°C hot plate in a ventilation hood until dried. The powder is then crushed with a mortar and pestle to ensure that no agglomeration persists. The powder is then weighed and poured into a 1" die that has been cleaned with methanol and lubricated with a small amount of oleic acid. Powders are pressed at 18,300 psi for 3 minutes on a Carver Laboratory Press. Sufficient pressure was determined based on the ability of the pellet to hold its shape after being pressed. A pressure too low introduces mechanical stresses and cracking. A pressure too high, and the pellet will not hold together when removed from the die. The green densities of the pellets are measured before sintering.

Another important parameter to ensure proper dopant concentration is to monitor pellet mass before and after sintering. If there is a significant amount of mass loss, then the measured dopant concentration of the pellet is not reliable. For the optimized deposition condition, mass loss during sintering was less than 1%, and thus not significant.

2.1.2 Methods for Pellet Sintering

A very important consideration when using PLD is target density. Thus, our GZO pellets must be sintered for densification[51]. If a target is not sufficiently dense, the energy density of the laser will cause particulate matter to be present in the subsequently deposited films. To minimize this occurrence, sintered GZO targets are required to be 95% or better than the theoretical density of ZnO.

Before sintering, a platinum foil is placed on a ceramic crucible to prevent undesired reactions from occurring. Some loose ZnO powder is sprinkled onto the platinum to protect the pellet from further impurities in the furnace. Sintering temperatures are typically around two thirds of the melting point of the material[52]. Sintering was performed in air at 1150C for 3 hours with a ramp rate of 4.7C/min. This temperature, 58% of ZnO's melting temperature of 1975C, was adequate to obtain sufficiently dense targets. Resulting targets are yellow or white in color. After sintering, targets are polished using sandpaper. They are sanded after each ablation as well, to avoid forming laser tracks, which alter momentum of the particles in the plasma plume. Target densities are measured to ensure that they are 95% or better than the theoretical density.

Table 2 shows conditions and pellet outcomes for various pressing and sintering conditions.

Table 2 Target preparation conditions

	Preliminary targets	**Intermediate attempt #1**	**Intermediate attempt #2**	**Final conditions**
Mixing conditions	Mortar and pestle	12hr ball mill in IPA	12hr ball mill in IPA	12hr ball mill in IPA
Mechanical Press	8000lbs/1min	14,000lbs/1min	15,500lbs/1min	15,000lbs/1min
Firing conditions	1hr at 1000°C	3hrs at 1000°C	3hrs at 1000°C	4hrs at 1150°C
Final condition	Low density	Low density	Stress cracking present	**95-99% dense**

2.2 Substrate Preparation

Preparing substrates for which optical and electrical properties are of key importance involves taking special care to remove dust particles and organic impurities on the substrate surfaces. Hence, cleaning is necessary prior to thin film deposition. The first part of this chapter will discuss cleaning procedures.

For contact resistivity measurements, films must be deposited in specific and known patterns in order to correctly measure and calculate specific contact resistivity. In order to create these patterns, whose details are on the scale of microns, photolithography is employed. The latter part of this chapter will discuss the circular transmission line method (CTLM) and photolithographic processes.

2.2.1 Substrate Cleaning

As mentioned, special care must be taken to remove dust particles and organic impurities on substrate surfaces to ensure optimum optical and electronic properties of a thin film. Any imperfections may lead to a loss in transparency and reduction in conductivity. In addition, these impurities may hamper nucleation and growth of thin films. The cleaning procedure is as follows. Substrates were first put into a 1:1 VersaClean : DI H_2O solution and ultrasonically agitated for 10 minutes. This was followed by a 10-minute ultrasonic bath in DI water, and then a 10-minute ultrasonic bath in acetone to remove particulates. The last 10-minute ultrasonic bath was in isopropanol to remove the acetone. Substrates were then dried with high purity nitrogen and placed in a UVO Cleaner, an ozone-cleaning device, for 10 minutes[53]. This is the end of the cleaning procedure for glass substrates. For silicon substrates, however, a native oxide layer is present. In order to remove this passivating layer, a 10-second, 1% HF dip is performed immediately prior to the substrate's insertion into the deposition chamber[54].

2.2.2 CTLM patterning via Photolithography

Realizing good ohmic contact is an important parameter to obtain efficient semiconductor devices. To determine how well or poorly the metal contacts the semiconductor, it is advantageous to choose particular contact structures that allow for measurements which quantify the contact quality. The type of structure chosen and the

ways in which measurements are made will be described in a later section. This section describes the process for patterning such structures to allow for the proper metallization of contacts, and thus later for contact resistivity measurements.

The photolithographic technique involves using a polymer-based photoresist which exhibits crosslinking upon exposure to UV light, or which breaks down under UV light, depending on the type of resist (negative or positive, respectively). Many photolithographic methods exist to accomplish various goals via photolithography. Some deciding factors include desired feature size, type of metallization to be performed, throughput speed, mask reuse, among others. Photolithography has many variable parameters, such as number of photoresist coats, spin speed and time, baking temperature and time, exposure time, develop time, and the order of the processes. The procedure followed for these experiments involves a process called "reverse image" which entails creating photoresist walls at feature edges which have an inverse trapezoidal shape (undercut), providing the ability to deposit metal onto the substrate while still leaving some of the photoresist exposed, making the photoresist lift-off process easier. The procedure adapted from MicroChem[55] is outlined below.

Photolithography was performed using a Laurel Technologies model WS-400A-6NPP/LITE spincoater. Samples were initially heated to 115°C for at least 5 minutes to ensure evaporation of any liquid on the surface. Then, AZ5214E photoresist was put on the sample and the sample spun for 50 seconds at 2500 rpm, followed by a post-exposure bake at 90°C for 2 minutes. The sample was then spun and baked in the same

manner, followed by two similar runs, but for 50 sec at 4700 rpm. Then the sample was subject to a 110°C bake for 50 seconds before a 0.2 second flood exposure to UV light (without a mask), using a Karl Suss MJB-3 Mask Aligner. The sample was then baked at 115°C for 2 minutes, and then exposed for 90 seconds with a mask. The sample was then submerged in Microposit MF-319 developer for 3 minutes, rinsed in DI water, and blown dry with N_2. The resultant photoresist mask was 1 um thick, allowing for up to 1 μm of metal deposition. This procedure leads to angled, "undercut" photoresist walls as described above, and shown in Figure 14.

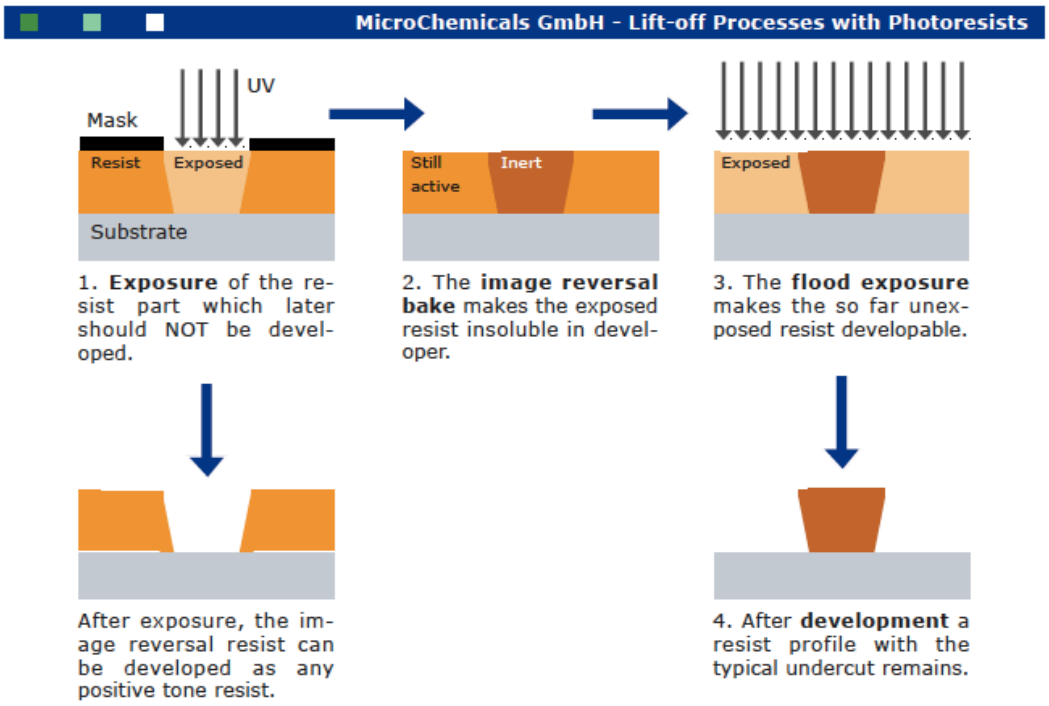

Figure 14 MicroChem procedure for creating reverse image photoresist patterns[55]

After metal deposition, samples were submerged in 80°C dimethyl sulfoxide (DMSO) for 3 minutes (or longer for thick metal depositions) and then agitated ultrasonically to remove the photoresist and any metal on top. It is important to be sure that there is no residual photoresist after developing, as this would cause inconsistencies in the metal deposition after lift-off, as anything deposited on top of this resist would be lifted off during photoresist removal.

Figure 15 shows a simplified process flow diagram for producing metal features on a substrate.

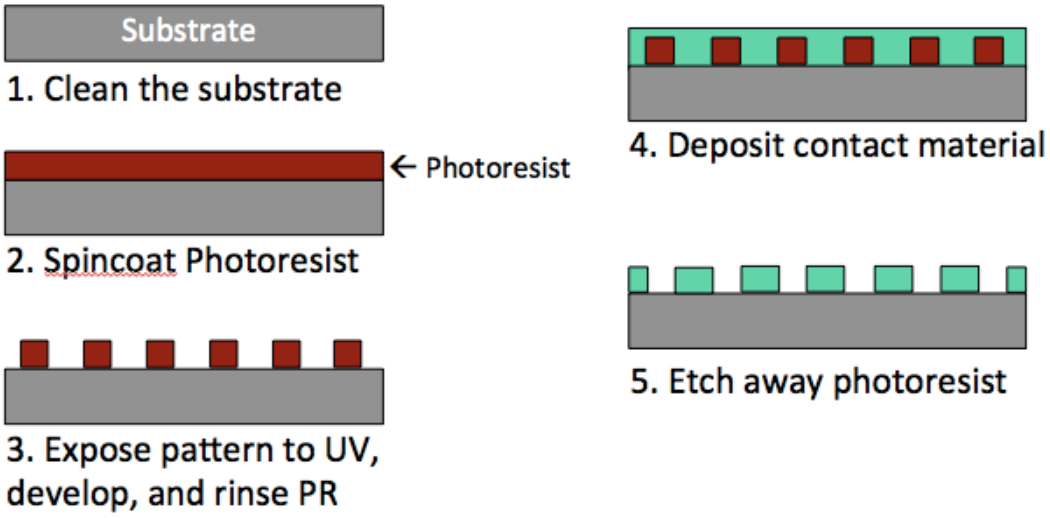

Figure 15 Cross-sectional views of the photolithographic process and subsequent metal deposition

2.3 Film Growth by Pulsed Laser Deposition (PLD)

A pulsed laser deposition chamber consists of a vacuum chamber in which there is a target holder/rotator facing a substrate holder/rotator/heater. There are also gas inlets that control the gas present in the chamber and the subsequent pressure constituting the deposition environment. A window into the chamber allows the entrance of a pulsed laser that hits the target, liberates atoms from the ceramic target material, and creates a plasma plume that travels to the substrate, onto which a thin film is grown. Laser pulses are generated using a Coherent Compex Pro 102 excimer laser with Kr-F gas mixture. Background pressures of 1.0×10^{-5} Torr or lower were achieved before deposition. The pulses of light incident on the target material causes some of the target to ablate, resulting in a plasma of energetic atoms that collide with and land on the substrate, where the material is reabsorbed as a film. A ZnO target containing a chosen amount of gallium oxide (Ga_2O_3) was positioned 10 cm away from the substrate, with the plume offset from the center of the rotating substrate holder so as to maximize the thickness uniformity[42]. Optimized transparent, conductive films were produced using an oxygen background pressure of 5 mTorr. Both target and substrate are rotated during deposition. Films for the optimization studies were prepared from 5600 laser shots at 250 mJ with a repetition rate of 10 Hz and a spot size of 8 mm x 3 mm, yielding 200 nm thickness, or approximately 0.35 Å/pulse. A schematic of the PLD chamber is shown in Figure 16.

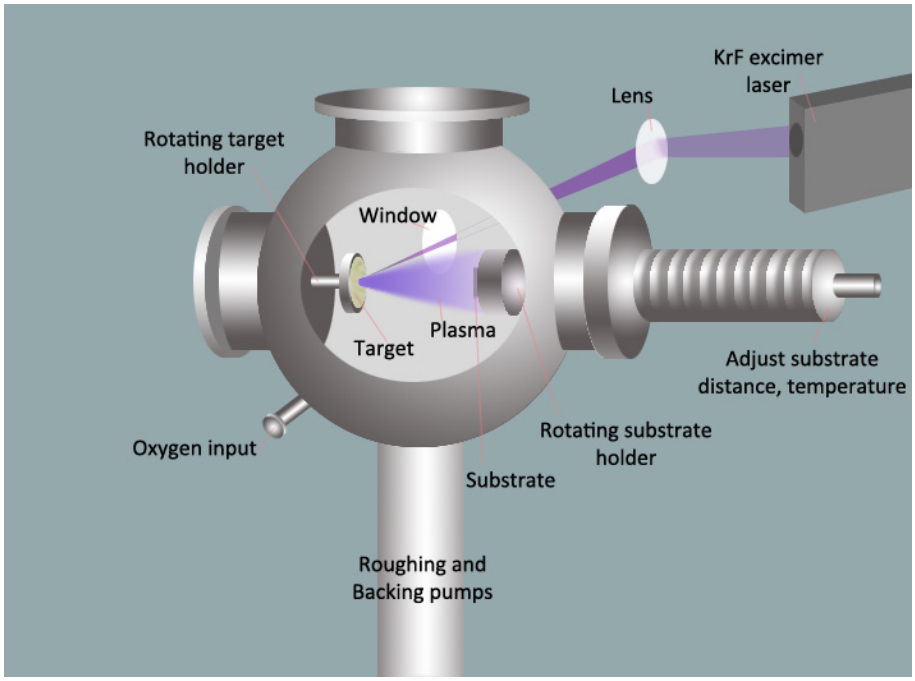

Figure 16 Schematic of the pulsed laser deposition chamber

2.4 Annealing

Material phases and compositions are highly dependent on the temperature and pressure under which they are held, as well as how long they are held there. One way to change the properties of materials is to anneal them in a particular environment. For these experiments, a tube furnace with a C&M, Inc. shell and Micropyretics Heaters International, Inc. heating elements is used to heat samples in a reducing environment, namely forming gas of a 1:99 H_2:N_2 composition.

2.5 DC Magnetron Sputtering of Reference Metals

To fabricate front silver contacts[56] as well as back aluminum contacts, metals were deposited via direct current (DC) Magnetron sputtering. Both of these metals are well-known and often used contact materials produced through sputtering[57].

An argon source is attached to the chamber and the internal argon pressure is controlled via a butterfly valve. The argon atoms, combined with a direct current source provides energy for the argon atoms to bombard the metal target, displacing the target atoms and creating a plasma plume which incidentally forms a film on the substrate below. Silver films were deposited using 20 W and 20 mTorr Ar pressure at a target-substrate distance of 1.75" for a deposition rate of 100 nm per minute. Aluminum was sputtered using 30 W and 12 mTorr Ar at the same target-substrate distance for a deposition rate of 25 nm per minute.

2.6 X-ray Diffraction (XRD)

X-ray diffraction (XRD) was employed to obtain structural analysis of our deposited films, as well as to examine the changes in crystallinity of ceramic targets with varying amounts of added dopant[58]. Film crystallinity was analyzed using a Panalytical Empyrean 4-circle diffractometer with parallel beam optics operated at 40 kV / 20 mA. Typical scans were collected for 15 minutes. Powder diffraction file cards from HighScore Plus were used to identify relevant phases. Peaks have been labeled using a single reflection notation.

2.7 Profilometry

The antireflective properties of films are highly dependent upon film thickness, as the thickness at which antireflection is possible is an odd multiple of a quarter wavelength of the incoming light, so precise and accurate measurement of thickness is of great importance. A Veeco Dektak 150 profilometer was used to measure thin film topography on the nanometer to micrometer scale. Profilometer measurements were performed to calculate deposition rates of all deposited films.

2.8 UV-vis spectrometry

To understand transmissive and reflective properties of our films as a function of wavelength, we utilized a UV-visible spectrometer setup equipped with a Newport 6254 series UV-enhanced Xenon lamp, a Gooch and Housego OL IS-671-LED integration sphere, and a Gooch and Housego OL-770 multi-channel spectroradiometer. This setup allowed measurement of reflectivity as well as transmission, each as a function of wavelength.

2.9 Four-point probe and Hall effect measurements

The basic electrical semiconductor parameters are conductivity, resistivity, majority carrier concentration, and mobility. Electrical conductivity is a measure of how

well a material accommodates the transport of charge carriers. Resistivity is the reciprocal of conductivity, and is a basic parameter of the conductive properties of semiconductor materials. Another important thin film property, sheet resistance, refers to the resistance between two sides of a square and is independent of the area of the square so long as the area is much larger than the thickness of the deposited film.

To calculate sheet resistivity, four-point probe was used to measure sheet resistance and profilometry was used to measure film thickness. Measurements of sheet resistance were made using a Keithley 2400 SourceMeter and Keithley 2182A Nanovoltmeter. Another way of obtaining resistivity values as well as charge carrier and mobility is to use Hall effect measurements. Four-point probe and Hall effect measurements will be discussed below.

2.9.1 Four-point probe

Four-point probe measurements calculate the resistivity of a coating by measuring the voltage between two inner probes while a current is passed between two outer probes. A constant current passes through two outer points and the difference in voltage is measured by a voltmeter.

The resistivity of the material is found from the following equation:

$$\rho = \frac{Wd}{L}\frac{V}{I}$$

where W is width, d is film thickness, and L is sample length. *V* is the difference in potential between the two inner points, and *I* is the current that runs between the two outer points.

There are four springy metal points, arranged in a line, which can be lowered onto the semiconducting surface. A constant current is forced between two outer points, and voltage is measured between the two inner points. The current density is not uniform but can be corrected for geometry. If the thickness of the wafer is much bigger than the distance between the points, resistivity (in $\Omega - cm$) is:[59]

$$\rho = \frac{\pi}{\ln 2}\frac{V}{I}d = 4.53\frac{V}{I}d$$

The sheet resistance R_s (in Ω / sq) is:

$$R_s = \frac{\rho}{d} = 4.53\frac{V}{I}$$

For these experiments, a current of 4.53 mA was applied for convenient conversion from voltage measurements to Ohms/sq sheet resistance values. Sample thicknesses were measured using profilometry.

2.9.2 Hall effect

Hall effect measurements involve the Lorentz force, which refers to the force that an electron experiences when it moves along a direction perpendicular to an applied magnetic field. The forces act on the charge carriers, which include a drift

velocity opposite to the conventional current direction. The electrons get pushed along the force direction while the semiconductor loses its local neutrality. The side opposite to the force direction becomes depleted of charge, and the other side receives an excess charge. Thus there is a measurable voltage called the Hall voltage. This phenomenon, called the Hall effect, was discovered by E. Hall in 1874.

$\vec{F} = q\left(\vec{E} + \vec{v} \times \vec{B}\right)$ (Lorentz force)

Since v and B are perpendicular, the resulting force is also perpendicular to both. A constant current (I) flows along the x-axis in the presence of a magnetic field along the z-direction. The transverse hall voltage is then:

$$V_H = \frac{IB}{qnd}$$

where q is the elementary charge of an electron (1.602×10^{-19} C), n is the charge carrier concentration, and d is the sample thickness.

Sheet resistance can be determined by using the Van der Pauw resistivity measurement technique. The mobility of charge carriers measured by Van der Pauw's technique is called Hall mobility, expressed by the following formula:

$$\mu = \frac{|V_H|}{R_s IB}$$

where R_s is sheet resistance. [59a]

Van der Pauw's technique[60] can be used to obtain electrical resistivity, Hall mobility and carrier concentration of the semiconductor. The thickness of the sample must be much smaller than the distance between the contacts. Four leads are connected

to the four metal contacts on the sample and current is applied from contact 1 to 2 to get the positive current I_{12} and measure the voltage from contact 4 to 3 to obtain V_{43}. Reversing the current obtains another current and voltage group of measurements, I_{21} and V_{34}. The same method gives the rest of the current and voltage measurements, I_{23}, I_{34}, I_{41}, I_{14}, I_{43}, I_{32}, and V_{23}, V_{41}, V_{21}, V_{14}, V_{32}.

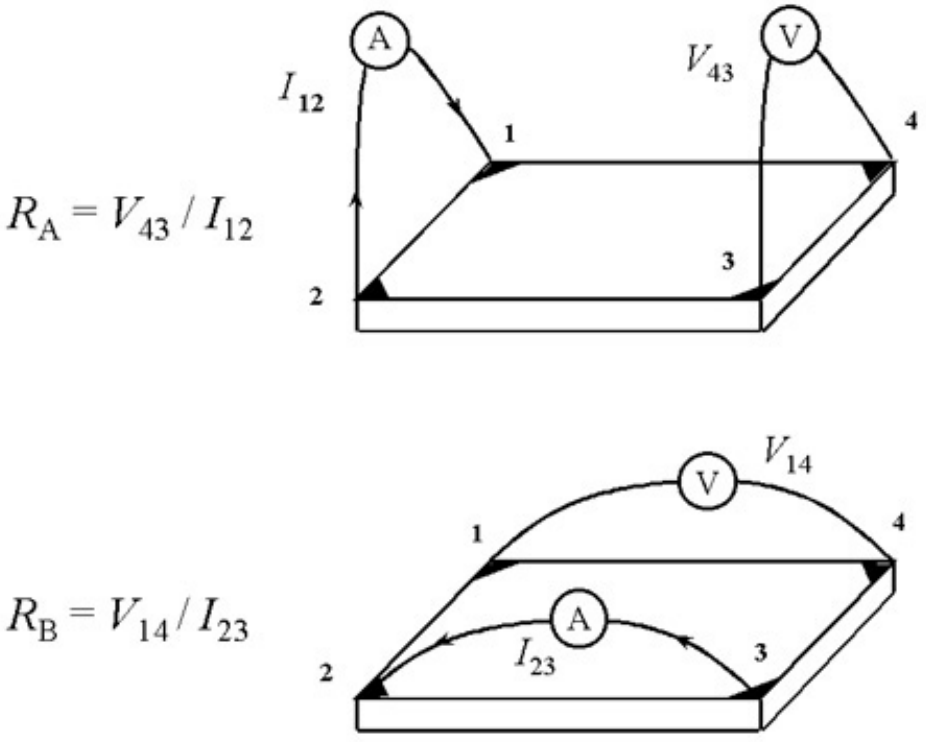

Figure 17 An example measurement using the van der Pauw configuration[60]

Resistance measurements can be calculated. $R_{21,34}=V_{34}/I_{21}$, $R_{12,43}=V_{43}/I_{12}$, etc. The sheet resistance R_s can be determined from the two characteristic resistances by the formula below:

$$\exp\left(-\pi\frac{R_A}{R_s}\right)+\exp\left(-\pi\frac{R_B}{R_s}\right)=1$$

where

$R_A=R_{21,34}+R_{12,34}+R_{43,12}+R_{34,21}$ / 4

And

$R_B=R_{32,41}+R_{32,14}+R_{14,23}+R_{41,32}$ / 4

If the conducting layer thickness d is known, the bulk resistivity can be calculated from R_s:

$$\rho = R_s d$$

Two sets of Hall measurements are made, one with positive magnetic field direction, and one with negative. Current is passed through a two diagonal leads, while Hall voltage is measured between the opposite diagonal leads. For example, current passed from lead 1 to lead 3 is I_{13} and the voltage measured between leads 2 and 4 with a positive magnetic field is V_{24P}. The sample type (n- or p-) can be determined from the Hall calculation of $V_C+V_D+V_E+V_F$ where

$V_C=V_{24P}-V_{24N}$,

$V_D=V_{42P}-V_{42N}$,

$V_E=V_{13P}-V_{13N}$,

$V_F=V_{31P}-V_{31N}$.

If the voltage is positive, the sample is p-type, and if negative, n-type.

The sheet carrier density (in cm^{-2}) is also calculated from these Hall voltages:

$$n_s = \left| \frac{8 \times 10^{-8} IB}{q\left(V_C + V_D + V_E + V_F\right)} \right|$$

where B is the magnetic field in gauss (G) and I is the dc current in amperes (A).

If the sample's conducting layer thickness d is known, the bulk carrier density can be determined:

$n=n_s/d$

Hall mobility (in $cm^2V^{-1}s^{-1}$) is calculated as follows:

$$\mu = \frac{1}{qn_sR_s}$$

An Ecopia Hall Effect Measurement System HMS-3000 was used to perform these measurements.

2.10 Ellipsometry

Ellipsometry measurements were made to examine the refractive index of our materials. A Wollam VASE Ellipsometer was used with a Hg-arc lamp source and attached monochromater. Ellipsometry measurements have been made on materials similar to the ones explored in this thesis[61].

2.11 Two-point probe specific contact resistivity measurements

Many methods exist to calculate contact resistance and specific contact resistance of metal contacts to highly doped semiconductors, but each method has its merits and limitations. One such method, the Transfer Length Method (TLM) proposed by Shockley in 1964[46], involved straight-line contacts along the sample, to which contact could be made and contact resistance and specific contact resistivity calculated. To do this, a DC current source and voltmeter are used to apply a constant current through the structure, during which a voltage drop will is induced over the two contacts and the semiconductor. Two probes measure this drop. Subsequent contacts at varying distances apart can be measured, for which a graph of distance apart vs. resistance between the contacts can be made. There will exist a linear relationship between the resistance and gap spacing between the contacts, which can be used to calculate contact resistance and specific contact resistivity[62].

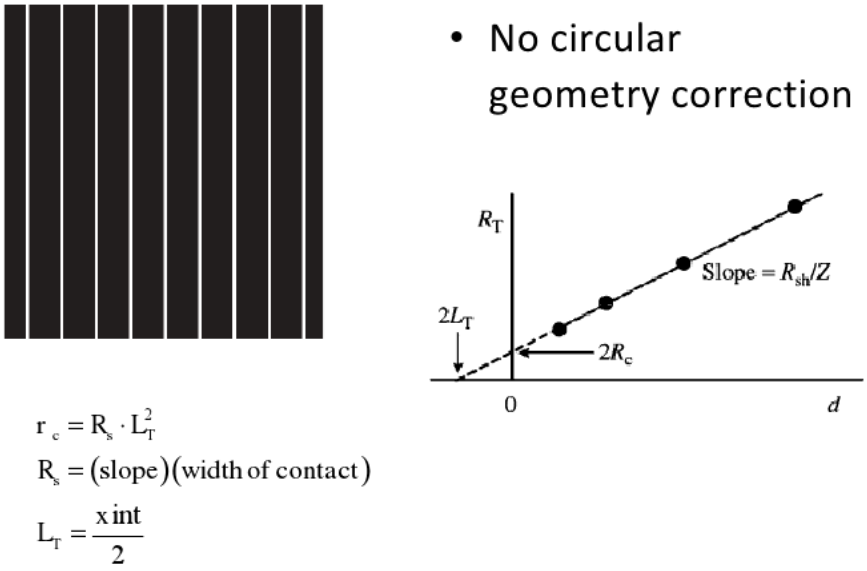

$$r_c = R_s \cdot L_T^2$$

$$R_s = (\text{slope})(\text{width of contact})$$

$$L_T = \frac{x\,\text{int}}{2}$$

Figure 18 Sample TLM wafer as well as graphical relations and equations[63]

The y-intercept yields 2*R, in which R is the contact resistance. Multiplying this resistance with the contact area yields the normalized contact resistance in Ohm-cm. the x-intercept yields two times the transfer length. The transfer length is a measure of the quality of the metal contact. Shorter transfer length indicates better contact. From the slope, the sheet resistance of the semiconducting layer can be calculated[64]. Using these values, the specific contact resistivity can be calculated as follows:

$$\rho_c = R_{sheet} L_T$$

in Ohm-cm^2.

This method, however, allows currents from one contact to another to spread due to current crowding. To circumvent this issue, the circular transfer length method (CTLM) was developed. In this method, concentric, circular contacts are formed via photolithography (which will be explained later in this section), and measurements are

made in a similar manner. For the calculation process, however, a simple geometry correction must be made, and then the contact resistance and specific contact resistivity calculations follow in the same manner as for TLM structures.

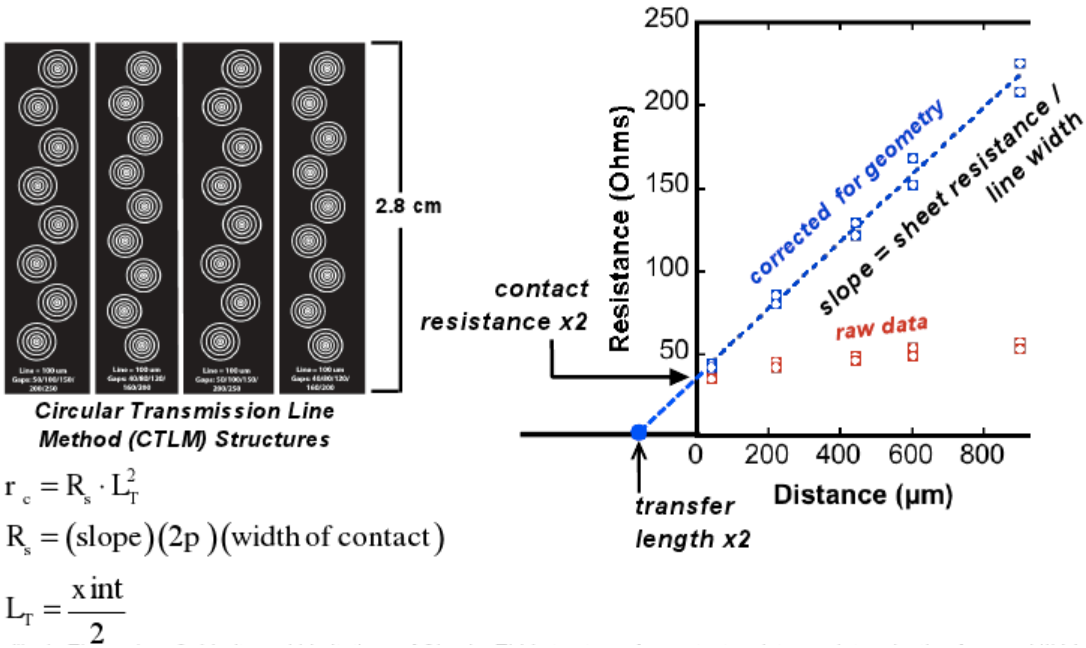

Figure 19 Sample CTLM wafer as well as graphical relations and equations[65]

Specific contact resistivity is determined using sets of resistance vs. distance measurements taken at constant current with increasing ring separation. CTLM structures allow us to extrapolate and extract contact resistance, transfer length, and sheet resistance values from a linear fit of resistance vs. distance data. From this data, ρ_c can be calculated. By measuring the total resistance for systematically increasing gap spacings and using a geometrical correction factor to compensate for the difference between linear and circular contacts, a linear fit is made to the experimental data.

Without the correction factor, CTLM underestimates the value of ρ_c[66]. The raw data is calculated, via $R_{raw}=V_{out}/I_{in}$ where I_{in} is the current input, usually 1 mA, and V_{out} is the resultant output voltage. The correction factor for each ring follows the formula $c_i = \frac{r_{center}}{r_i}\ln\left(\frac{r_{center}+r_i}{r_{center}}\right)$ where r_{center} is the radius of the inner contact and r_i is the distance from the center contact to the ring being measured where i=1,2,3,4 or 5 for the ring number. Then the corrected resistance $R_{corr} = \frac{R_{raw}}{c_i}$ yields data suitable for linear fitting.

One can then plot R_{corr} vs. r_i and fit to a line, where the data follows the form $R_{corr} = m \cdot r_i + b$ where m is the slope of the line and b is the y-intercept. The fit should have a χ^2 value of 0.99 or better to ensure the data is reliable. From the linear data fit, one can extract the sheet resistance, transfer length, and thus specific contact resistivity. Since no annealing processes were employed during this experiment, it is reasonable to assume (as required by the any TLM method) that the sheet resistance of the material under the contacts has not been altered significantly and is comparable to the sheet resistance away from the contact metal[63]. As such, sheet resistance values extracted graphically can be compared to sheet resistance values measured experimentally via four-point probe to validate the analysis. From the sheet resistance and the transfer length, specific contact resistivity can be calculated. The equations governing each are given below:[67]

Sheet resistance: $R_s = m \cdot 2\pi \cdot r_{center}$ where r_{center} is in μm, m is in ohms/μm, and R_s is in ohms.

Transfer length: $L_T = -\frac{b}{m} \cdot \frac{1}{2} \cdot \frac{10^{-4} cm}{\mu m}$ where b is in μm, m is in ohms/μm, and L_T is in cm.

Specific contact resistivity: $L_T = -\frac{b}{m} \cdot \frac{1}{2} \cdot \frac{10^{-4} cm}{\mu m}$ where R_s is in ohms, L_T is in cm, and ρ_c is in ohm-cm^2.

3. Manuscript

Ga-doped ZnO thin films for conducting antireflection coatings

N.A. Estrich, D. H. Hook, J.T. Leonard, *Brian J. Laughlin, Ian Cooper, and J-P. Maria

North Carolina State University, Department of Materials Science and Engineering, Raleigh, NC, *Dupont Microcircuit Materials

Abstract

This letter reports an evaluation of transparent, conductive gallium-doped ZnO (GZO) thin films for a conducting antireflection coating appropriate for crystalline silicon solar cells as a means to enhance efficiency by reducing the overall resistivity of the photovoltaic circuit. All Ga-doped ZnO thin films in this study were deposited using pulsed laser deposition. Synthesis conditions were first optimized for maximum electrical resistivity and minimal visible light absorption. The ideal combination was 1 wt% Ga, 90% transmissive in the visible range, with resistivity in the $1x10^{-3}$ ohm-cm range. Optimized films were prepared on reference flat silicon wafers with known dopant densities and on commercially available solar cell substrates. These GZO layers were patterned for circular transmission line method

(CTLM) measurements of specific contact resistivity (ρ_c). For textured *n*-emitter cells, contact resistivity values of 2 mohm-cm^2 were observed routinely. These values are consistent with, or lower than contact resistivities associated with conventional silver-based metallization. In addition, prototype cells were fabricated and efficiency measurements were found to be 14%.

Introduction

Many modern microelectronic and photonic devices are dependent on low resistance, and ideally ohmic, contacts for efficient operation[68]. Contact characterization can be made by measuring specific contact resistivity (ρ_c), which describes the resistance per unit area associated with the barrier at a metal/semiconductor interface[63]. Specific contact resistivity is dependent upon temperature, barrier height, and impurity concentration and follows the relation:

$$\rho_c \propto \exp\left[\frac{2\sqrt{\varepsilon_s m_e^*}}{\hbar}\left(\frac{\phi_B}{\sqrt{N_D}}\right)\right]$$

where ε_s is the semiconductor permittivity ($\varepsilon_{s,ZnO}$=8.5), m_e^* is the effective electron mass, $\hbar$ is Planck's constant, ϕ_B is the Schottky barrier height, and N_D is the semiconductor donor concentration. Low contact resistivity values occur when barriers are low, and more importantly narrow. Narrow barriers are associated with very high semiconductor dopant densities[69] which is typically the case for modern silicon solar cells that feature most commonly *n*-emitters with phosphorus concentrations above $10^{20}/cm^3$ at the immediate surface[70]. However, following demands for increased efficiency, emitter dopant densities are being reduced to enhance capture of the lower wavelength segment of the solar spectrum (*i.e.*, the blue response) despite the penalty of a higher overall cell resistance. Increasing the contact area can reduce resistivity values, however, this comes at the expense of eclipsing more of the active cell. This tradeoff can be overcome by either developing contact metallurgies that have lower barrier heights, or by developing contacts that are transparent.

The challenge of ohmic contacts to *n*-type silicon are well-known: there are sparingly few materials that create low barrier height contacts and that are consistent with the process flows used in modern solar cell manufacturing lines. These include requirements of extremely high throughput, minimal use of noble or rare metals, and ideally air firing. As such, we explore the alternative option of assistance by transparent contacts.

Antireflection coatings (ARCs) for solar cells establish the optical transition between air and the highly-doped silicon emitter. Much interest has been expressed in finding transparent, conductive ARCs for thin film solar cells. The current industry standard transparent conductive oxide (TCO) is indium tin oxide (ITO), however, due to the limited availability and thus high cost of indium, alternate materials have been sought out[71]. Zinc oxide (ZnO) is an inexpensive, abundant material that, when doped with group-III elements such as gallium, exhibits resistivity values below 10^{-3} ohm-cm. In addition, this wide bandgap II-VI semiconductor is highly transparent in the visible spectrum, deeming it an attractive candidate for antireflection coatings for solar cell applications. Current desires to enhance crystalline silicon cell efficiencies, to reduce emitter dopant densities, and to potentially eliminate all expensive materials (*e.g.* Ag, In) places renewed interest on conducting ARCs for conventional cells.

Various techniques have been employed to deposit ZnO thin films, including pulsed laser deposition (PLD), which is used in the present study as it presents a number of advantages for laboratory scale research. We note that ZnO films with comparable properties

can be prepared using multiple techniques, including those appropriate for large area film deposition.

Experimental Procedure

GZO films were prepared by pulsed laser deposition (PLD) using a Coherent Compex Pro 102 excimer laser with Kr-F gas mixture. A ZnO target containing 1 wt.% gallium oxide (Ga_2O_3) was prepared in-house by conventional powder processing techniques. A constant target-to-substrate separation distance of 10 cm was used for all depositions, with the plume axis offset approximately 5 mm from the center of the rotating substrate holder so as to maximize the thickness uniformity[42]. With this configuration 1" x 1" coupons with uniform thickness were possible. Both target and substrate were rotated during deposition. Films for the optimization studies were prepared from 5600 laser shots at 250 mJ with a repetition rate of 10 Hz and a spot size of 8 mm x 3 mm, yielding 200 nm thickness, or approximately 0.35 Å/pulse. Film crystallinity was analyzed using a Panalytical Empyrean 4-circle diffractometer with parallel beam optics, and optical property data was collected using a Gooch and Housego OL-770 multi-channel UV-visible spectrometer equipped with an 8 cm diameter Gooch and Housego OL 15-671-LED integration sphere. Carrier concentrations and mobility were measured using an Ecopia Hall Effect Measurement System HMS-3000, where Ga-solder was used to connect the sample to the gold pins of the Hall effect measurement system. Resistance measurements were made with a Keithley 2400 SourceMeter and Keithley 2182A Nanovoltmeter.

To accommodate circular transmission line measurement (CTLM) analysis, sets of concentric GZO rings were patterned using lift-off with the following procedure. Wafers were cleaned initially in an ultrasonic bath of water, then isopropyl alcohol, then acetone, then ethanol for 10 minutes each, followed by 10 minutes in an UV-ozonator and finally a 10 second, 1% HF dip to remove the native SiO_2 layer. The initial photoresist layer (AZ5214E photoresist) was patterned via the conventional photolithographic technique described by MicroChemicals[55]. For CTLM analysis, the starting substrate was a 2.75 cm x 2.75 cm coupon containing 34 CTLM structures, as shown in Figure 20[65]. In all cases, after deposition the resist was removed by submerging samples in 81°C dimethyl sulfoxide (DMSO) for 3 minutes followed by ultrasonication for 25 seconds, rinsing with methanol, and drying with nitrogen.

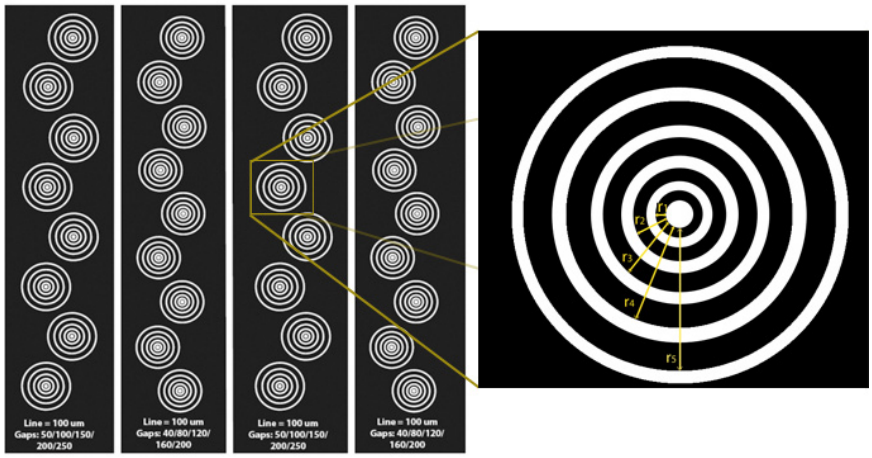

Figure 20 Mask for CTLM structures on a 2.75 cm x 2.75 cm wafer, and a close-up of one structure, with ring distances indicated

Silver films were prepared using the following sputtering conditions: a target-substrate distance of 1.75 cm, a 1" Ag sputtering target, 20 mTorr of Ar, and 20 W direct current (dc) power during a two minute deposition. These conditions produced 200 nm thick silver films.

Specific contact resistivity was determined by sets of resistance vs. distance measurements taken at a constant current of 1.00×10^{-3} amps with increasing ring separation. CTLM structures allow us to extrapolate and extract contact resistance, transfer length, and sheet resistance values. By measuring the total resistance for systematically increasing gap spacings and using a geometrical correction factor to compensate for the difference between linear and circular contacts, a linear fit is made to the experimental data. Without the correction factor, CTLM underestimates the value of ρ_c[66]. The raw data is calculated, via $R_{raw}=V_{out}/I_{in}$ where I_{in} is the current input, typically 1 mA, and V_{out} is the resultant voltage drop. The correction factor for each ring follows the formula $c_i = \frac{r_{center}}{r_i} \ln\left(\frac{r_{center}+r_i}{r_{center}}\right)$ where r_{center} is the radius of the inner contact and r_i is the distance from the center contact to the ring being measured where i=1,2,3,4 or 5 for the ring number (as shown in the close-up in Figure 20). The corrected resistance is then $R_{corr} = \frac{R_{raw}}{c_i}$. An example of raw CTLM data compared to data for which the correction factor has been applied is shown in Figure 21[65]. For the current structures, the minimum contact gap distance is 40 μm while the maximum contact distance gap is 1150 μm.

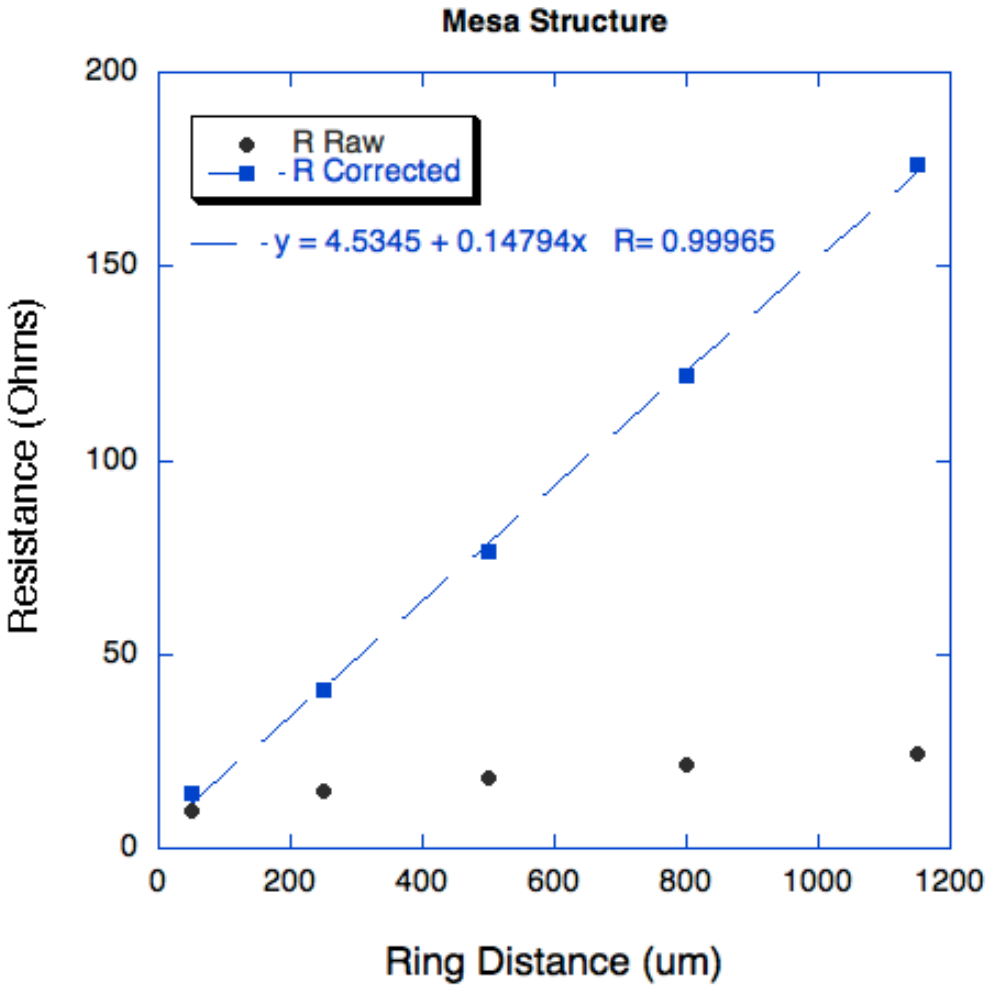

Figure 21 Plot of resistance vs. distance for a mesa structure, showing raw resistance data as well as data corrected for the geometry of the circular test structures

One can then plot R_{corr} vs. r_i and fit to a line, where the data follows the form $R_{corr} = m \cdot r_i + b$ where m is the slope of the line and b is the y-intercept. To ensure reliability of the data, we report only data for which the goodness of fit yields a χ^2 value of 0.99 or greater. From the linear data fit, one can extract the sheet resistance, transfer length, and thus specific contact resistivity[62a]. Since in this experiment the substrates were never annealed to

high temperatures, it is reasonable to assume (as required by the any TLM method) that the sheet resistance of the material under the contacts has not been altered significantly and is comparable to the sheet resistance away from the contact metal[63]. As such, sheet resistance values extracted graphically can be compared to sheet resistance values measured experimentally via four-point probe to validate the analysis. From the sheet resistance and the transfer length, specific contact resistivity can be calculated. The equations governing each are given below:[67]

Sheet resistance: $R_s = m \cdot 2\pi \cdot r_{center}$ where r_{center} is in μm, m is in ohms/μm, and R_s is in ohms.

Transfer length: $L_T = -\frac{b}{m} \cdot \frac{1}{2} \cdot \frac{10^{-4} cm}{\mu m}$ where b is in μm, m is in ohms/μm, and L_T is in cm.

Specific contact resistivity: $\rho_c = R_s \cdot L_T^2$ where R_s is in ohms, L_T is in cm, and ρ_c is in ohm-cm^2.

Results and Discussion:

1. ZnO optimization

Optimization of thin film deposition requires investigation of deposition pressure and its effect on crystallinity, resistivity, mobility/carrier density, and optical transparency of the deposited films. First, GZO films of constant 90 nm thickness were deposited onto smooth silicon substrates in oxygen ambient pressures of 1, 5, and 30 mTorr. The samples were analyzed via x-ray diffraction in the as-deposited state to determine crystallinity.

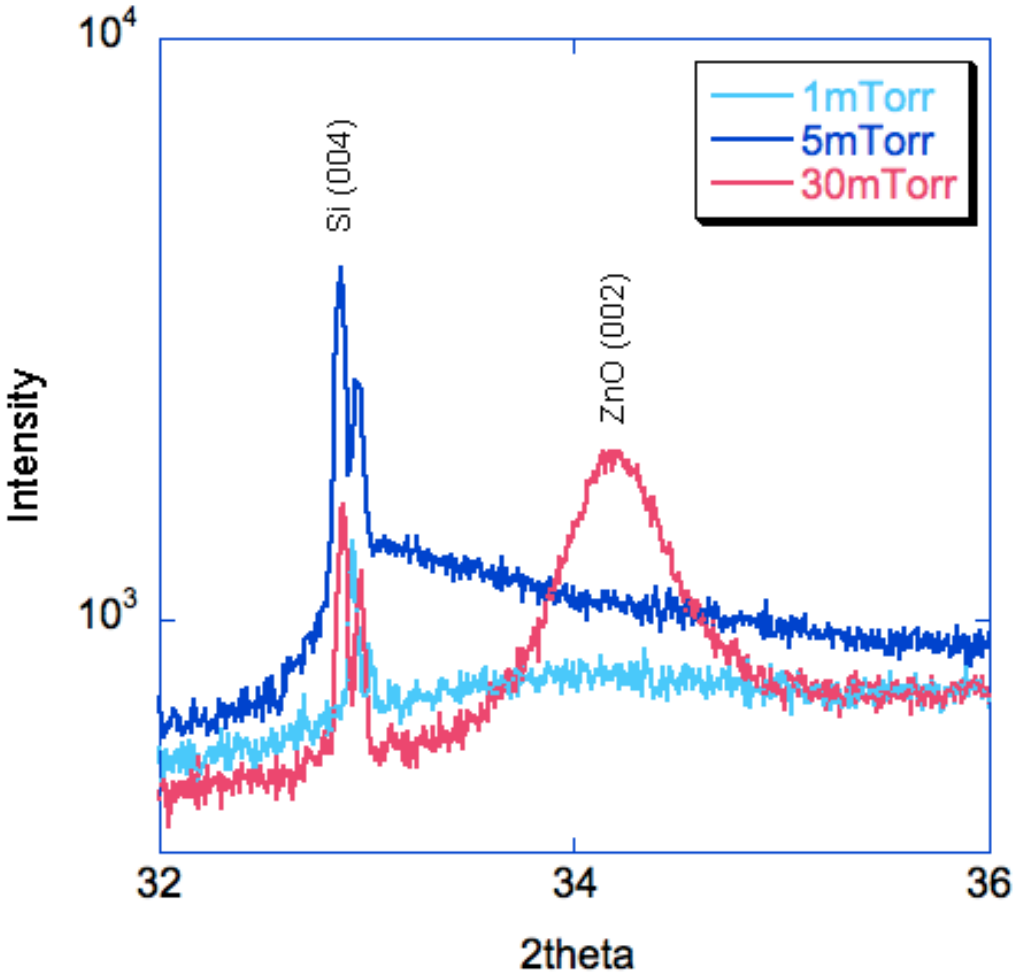

Figure 22 XRD data for 1 wt.% Ga-doped ZnO deposited onto (100) single crystalline Si substrates, deposited at varying oxygen deposition pressures

It is evident from Figure 22 that at room temperature and low deposition pressures, 1 wt.% Ga-doped ZnO is amorphous, while at higher deposition pressures (30 mTorr), films are crystalline.

To examine the effects of doping and annealing on crystallinity, a comparison is made by depositing undoped ZnO and 1 wt.% doped ZnO, each in a 5 mTorr oxygen

environment, and examining the crystallinity of each before and after annealing in forming gas.

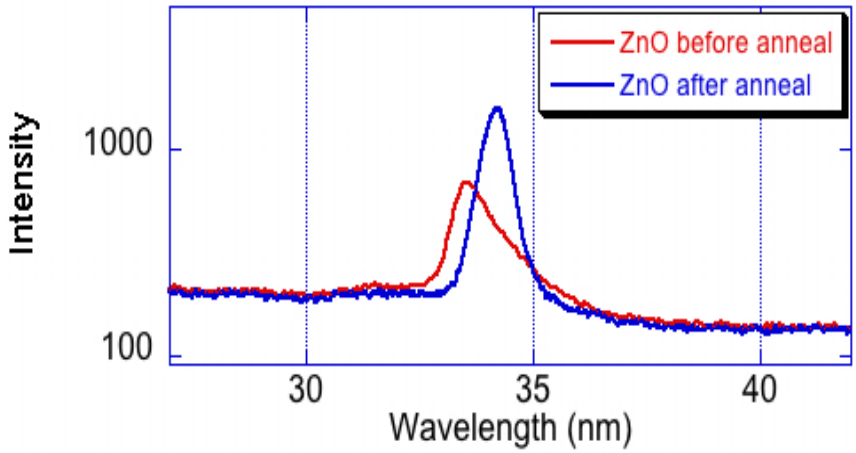

(a)

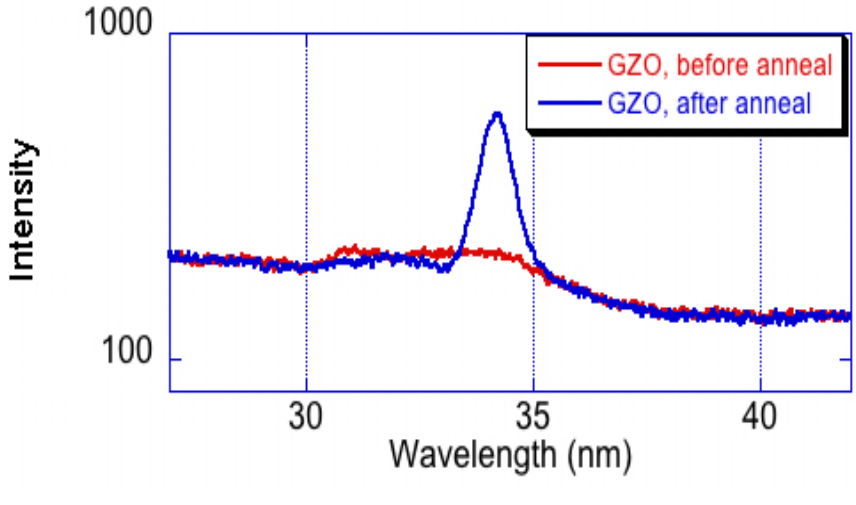

(b)

Figure 23 XRD plots of (a) Undoped ZnO and (b) 1 wt.% Ga-doped ZnO deposited at 5 mTorr O_2 pressure onto (100) Si, shown before and after forming gas annealing

While it is clear from Figure 23 that undoped ZnO deposited at a low deposition pressure at room temperature is in its crystalline state, Ga-doped ZnO deposited under the same conditions is amorphous, and that each is crystalline after annealing. Consequently,

ZnO films deposited at low deposition pressures at room temperature, do not contain widespread distributions of grain boundaries which may scatter electrons and perhaps act as recombination centers. Therefore, optimization of optical and electrical properties in low deposition atmospheres may prove a desirable attribute of these GZO films.

The next material parameters to be investigated as a function of deposition pressure were electrical resistivity, mobility, and carrier density. Again, films of 90 nm thicknesses were deposited onto glass substrates at oxygen deposition pressures ranging from 0.1 mTorr to 100 mTorr. A summary of the Hall measurement results are shown in Figure 24. The relationships between resistivity, carrier density, and mobility are self-consistent. We explain these observations following the model of Demchenko *et al*., where GZO synthesis at low oxygen partial pressures favors Ga occupation on a Zn site with charge compensation by electrons[72]. If the same Ga concentration of GZO is prepared under high oxygen partial pressures, Ga will still occupy Zn sites, but electroneutrality is met by a combination of electrons and vacant zinc sites. The V_{Zn}-Ga_{Zn} defect complexes serve a dual role to reduce overall electron concentrations and to reduce mobility via additional scattering.

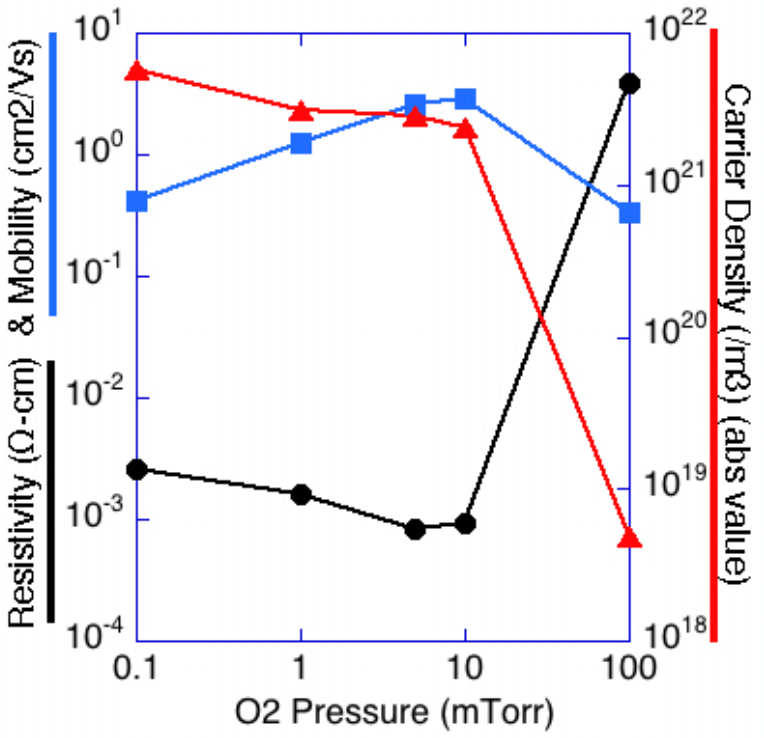

Figure 24 Hall measurement data, featuring resistivity, mobility, and carrier density as a function of oxygen pressure deposition environment

Electrical resistivity should be minimized for efficient cell operation, however not at the expense of optical transparency. This is particularly important for ZnO, where it is known that excessively reducing conditions (that generally favor high conductivity) also lead to absorption in the visible spectrum[73]. As such, it is necessary to optimize the optical properties, namely transparency, in conjunction with resistivity to identify the optimal balance. Films of 90 nm thickness were deposited onto transparent glass substrates at oxygen pressures ranging from 0.1 to 100 mTorr. Transparency measurements are shown in Figure 25.

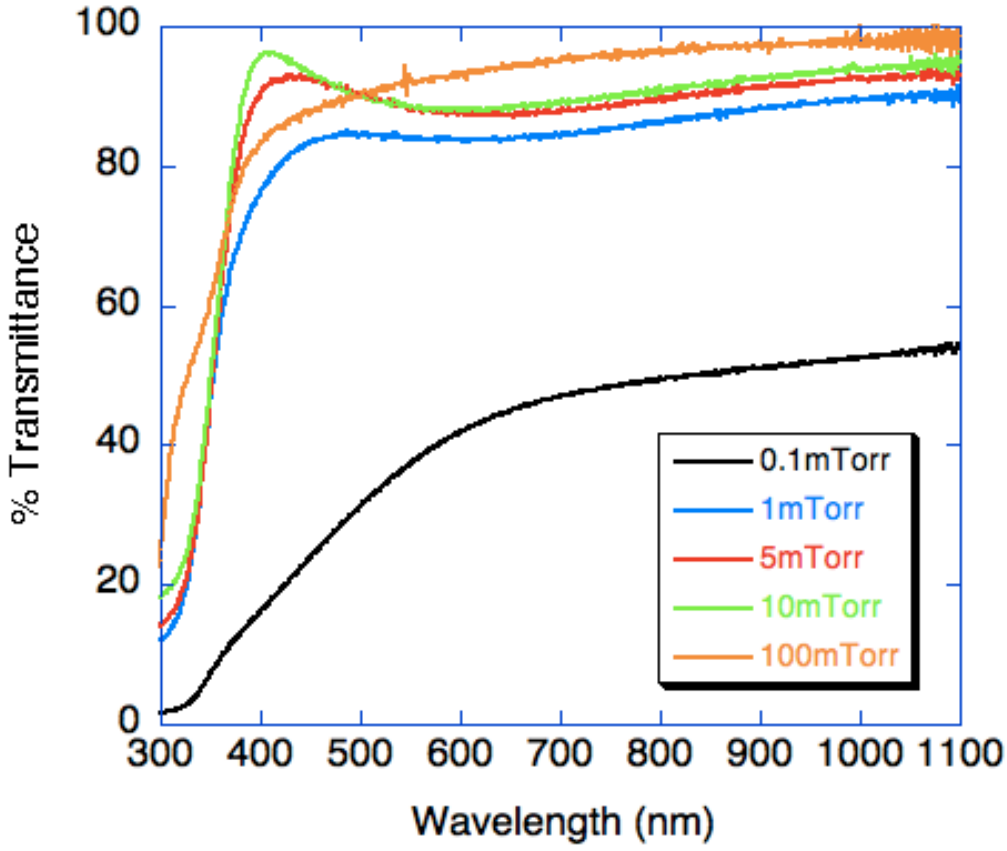

Figure 25 UV-vis measurements of transparency as a function of O_2 deposition pressure

It is obvious that at a deposition pressure of 0.1 mTorr, transparency is lower than desired and unsuitable for ARC applications. At deposition environments of 5 mTorr and above, transmission reaches approximately 90% across the visible and infrared wavelength range, which is sufficiently high for ARC applications[29-30]. At 100 mTorr, the shape of the transmission curve changes. We note that at this pressure, the plasma plume becomes

substantially narrower, causing a nonuniformity in film thickness that is larger than the optical probe. This thickness variation interferes with the expected interference intensity oscillations seen in the 1, 5, and 10 mTorr samples.

From the electrical resistivity and optical transparency data, we identify an oxygen pressure window between 5 and 10 mTorr where optical transparency is sufficiently high and electrical resistivity is sufficiently low. This window is valid for ablation from a ZnO target with 1 mol% Ga_2O_3.. The data are not shown, but a similar set of optimizations were made for ZnO targets with 2%, 4%, and 6% Ga_2O_3. In all cases trends were similar, but none offered a similarly attractive balance of optical and electrical properties.

2. Contact formation

To take into account the complications of *p-n* junctions and surface texturing present in solar cells, we examined contact resistivity on smooth silicon wafers and on naked monosilicon textured solar cells. The smooth silicon wafers are arsenic doped, with resistivity 0.001 Ohm-cm ($10^{19}/cm^3$). The exact dopant concentration at the emitter surface is unknown, however, the sheet resistance is 50 Ω/square. Three sets of contacts were evaluated: 1) ZnO with the optimized properties, 2) pure sputtered silver, and 3) mesa structures comprised of GZO capped with a silver layer. The commonly used metal for contacting n-type Si emitters is silver, thus the Ag contacts establish our context for comparison. The identical analysis was performed for all cases. For evaluation, we present in Table 3 the contact resistivity, the extrapolated sheet resistance, the goodness of fit (χ^2), and

the measured sheet resistance by four-point probe for each substrate. The comparisons of measured vs. extrapolated sheet resistance values offer reasonable validation of the CTLM approach and the geometric corrections.

Table 3. CTLM measurements: measured sheet resistance, expected sheet resistance (from four-point probe technique), transfer length, contact resistivity, and goodness of fit

Sample	R_s (Ω /sq)	R_s expected (Ω /sq)	L_T (cm)	ρ_c (m Ω - cm^2)	χ^2
Ag on smooth Si	360	17	0.024	200	0.991
GZO-mesa on smooth Si	10	17	0.012	1.4	0.997
Ag on textured Si	48	50	0.001	0.1	0.999
GZO-mesa on textured Si	47	50	0.001	0.1	0.999

The first experiment was a comparison of GZO and Ag contacts to smooth (100) Si. Pure Ag produced a contact resistivity of 200 mΩ-cm^2 while the GZO-mesa contact produced a value of 1.4 mΩ-cm^2. For the silver metal and the GZO-mesa contacts, the extrapolated sheet resistance values are 360 and 10 Ω/square respectively. The huge disparity observed for Ag indicates failure of the transmission line model. This is not unexpected for Ag considering the combination of a 10^{19}/cm^3 *n*-type Si and a substantial Ag-Si barrier height of ~0.7 eV. Berger concluded that such combinations would exhibit Schottky diode characteristics, leaving no opportunity for low contact resistivity[62a]. In contrast, for the case of GZO-Si, though much less rigorously established, the barrier height to *n*-type Si is expected to be between 0.4 and 0.5 eV, which translates theoretically to a contact resistivity of approximately 0.1 mΩ-cm^2. The experimentally observed contact resistivity is

approximately 14 times larger than theoretical while the extrapolated sheet resistance is of the same order. Agreement to theory is reasonable considering the proximity to dopant concentrations and barrier height combinations that preclude low resistance contact formation.

The same Ag / GZO-mesa comparison was made on commercial textured solar cells with substantially higher dopant concentrations. We note that the exact concentration is not known, but values above $10^{20}/cm^3$ are customary for the very surface. As expected for both materials the contact resistivity values fall to statistically (by averaging over many measurements) similar values of 0.1 $m\Omega\text{-}cm^2$. Measured and calculated sheet resistance values are within 5%, which give confidence to the CTLM method of contact resistivity extraction. Ultimately, this data suggests that a GZO ARC exhibits a contact resistivity value that is consistent with that needed for front-face contact. By considering total resistive losses, Schroder estimates that contact resistivities should be lower than 2 $m\Omega\text{-}cm^2$, which is substantially larger than the numbers reported presently[45b]. We speculate that a similar requirement would be present for the currently proposed application of a conducting ARC rendering them a useful new option to the photovoltaics community.

As a final step in this research, the GZO ARCs were evaluated in the final embodiment of a fully fabricated solar cell. The first step in this process required identifying the layer thickness that optimizes light capture. To determine the appropriate range for ARC thickness, a series of films were made on the textured, monocrystalline solar cell wafers with increasing total thickness. For reference, we measured in parallel an uncoated and textured

wafer and a textured wafer with a commercial grade SiN_x ARC. Reflectivity vs. wavelength measurements were made on this series using a UV-vis spectrometer with an integration sphere. The results are shown in Figure 26.

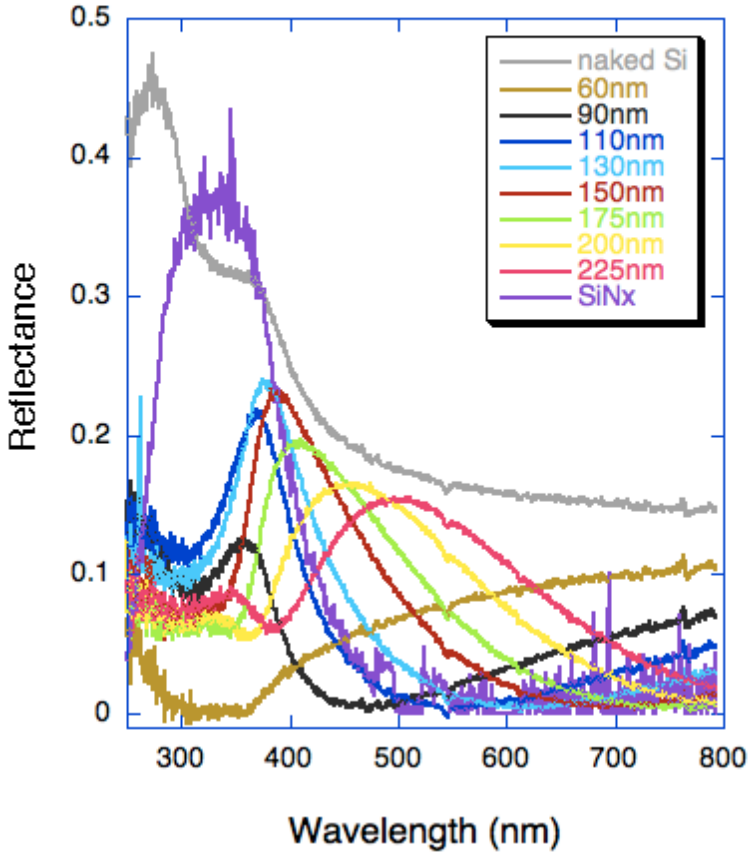

Figure 26 Reflectance vs. Wavelength data for GZO films varying from 60nm to 225nm on textured, monocrystalline Si solar cells, as well as a solar wafer with no ARC present (naked Si). Also included is a SiNx ARC on the same type of substrate.

The data in Figure 26 reveals that all thicknesses of GZO on the solar cell wafers improve antireflection properties when compared with the uncoated wafer. The GZO film thickness offering the broadest band improvement in light capture lies between 90 nm and 130 nm. In this range, the reflectance data between GZO and a commercial ARC (also plotted) are comparable. This thickness range is consistent with SiN_x that exhibits a similar refractive index of 2.02 and a similar optimized thickness of 90 nm in this case[74]. We note that thickness uniformity for our PLD thin films is insufficiently large to cover the sampling area of the integration sphere with perfectly thickness-uniform material. Consequently, there is a limit to achieving an ideally low reflection over a broad wavelength range. The UV reflectance is much lower for ZnO given its lower bandgap and onset of absorption. This, however, lies outside of the pertinent range for Si-based solar cells.

Prototype solar cells were fabricated to measure efficiency and ideally determine the extent to which a conducting ARC contributes to electronic transport. Cells were fabricated starting with naked, monocrystalline commercial-grade solar cells with a *p*-type bulk, and a highly doped *n*-emitter, the surface of which exhibits standard anisotropic etching texture 3-5 microns in height. Back contacts were first fabricated by screen-printing DuPont PV381 Al-based paste, drying at 150°C for 10 minutes, then rapid-firing to a peak temperature of 930 °C. The cell faces were then exposed to a 1% HF dip to remove any native oxide layer. A GZO ARC was deposited over the entire cell using the optimized pulsed laser deposition conditions to a 90 nm thickness. A front face metallization of a grid and busbar pattern was fabricated in two ways: 1) by a standard lift-off process (reference please) in which pure Ag was sputtered to a thickness of 1 μm, and exposure to acetone in an ultrasonic bath

completed the lift-off process, and 2) in which the grid and busbar pattern were formed by standard screen printing of DuPont PV17S, and subsequent drying at 150 °C then firing in air using a standard fast fire profile with maximum temperature of 850 °C.

Efficiency measurements were made using an ST-1000 Current-Voltage Tester by Telecom-STV Ltd. Results from this experiment are shown in Figure 27.

Front contact	Eff (%)	FF	Voc	Isc
Sputtered Ag	11.1	64.1	0.59	0.25
DuPont PV17S	13.6	69.1	0.59	0.27

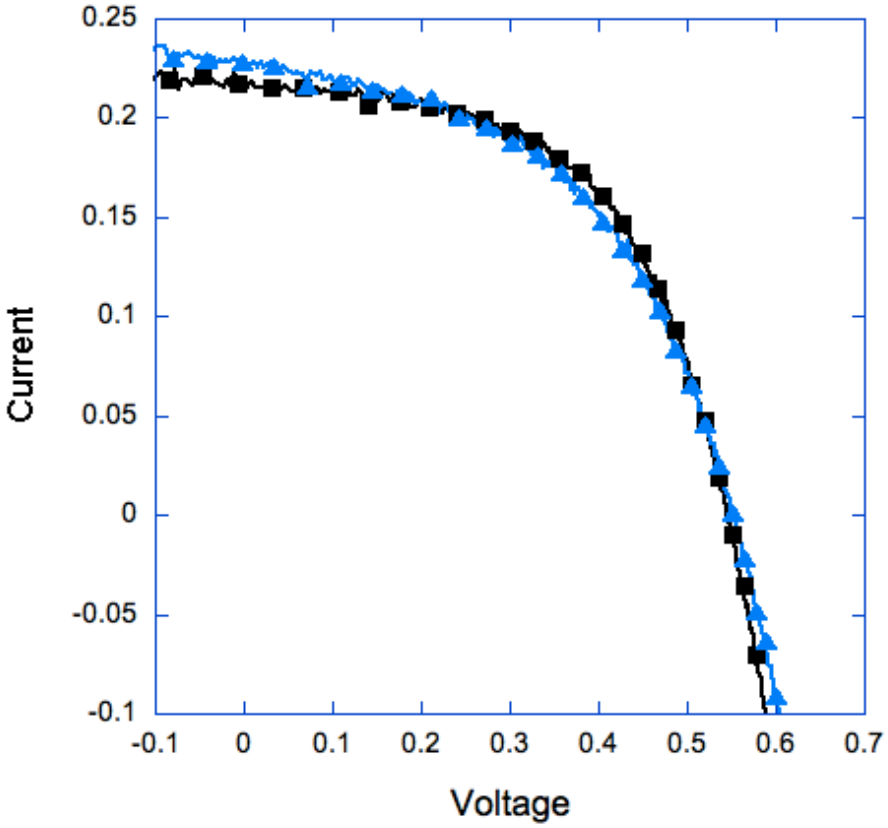

Figure 27 Current-Voltage measurements for two samples: Black (square marker) data corresponds to cells with sputtered Ag front contacts. Blue (triangle marker) data corresponds to cells with DuPont PV17S screen-printed front contacts. Corresponding efficiency, fill factor, open circuit voltage, and short circuit current are reported for each. (Color available online.)

Efficiencies of 14% were measured for these devices. While the efficiency numbers for this experiment are modest, we have demonstrated proof of concept. It is important to note that the Ag metallization grids and busbars are isolated from the emitter in all areas, so

all of the photocurrent is passing through the GZO conductor. It is also important to note that the emitters in all of these cell experiments were un-passivated, and it is known that passivation of similar cells should produce a 3% or greater increase in cell efficiency. Furthermore, it is likely that a proper engineering optimization (which is outside the scope of the present work) would provide additional gains. As such, it is sensible to expect that efficiency numbers in the competitive range of 17% to 18% are entirely possible.

Conclusions

The suitability of gallium-doped zinc oxide to serve as a conductive antireflection coating was demonstrated. GZO thin films were prepared by PLD with conductivity values in the range of $1x10^{-3}$ Ω-cm and transmission values greater than 90% in the pertinent spectral range. CTLM analysis revealed a contact resistivity value for GZO to a highly doped n-emitter of 0.1 mΩ-cm^2, a value comparable to that achieved with pure Ag, and better than achieved conventionally with standard Ag-based paste electrodes. The GZO films exhibited reflectivity (and thus light capturing ability) on textured monocrystalline solar cells that is comparable to a commercially-available SiN_x ARC. A series of solar cells were fabricated using GZO antireflection coatings. Efficiency cells in the range of 14% were achieved. Though modest, these numbers are promising as they were achieved without significant process optimization or emitter surface passivation. Importantly, these results suggest that ZnO ARCs are compatible with conventional Ag-based fire-through pastes and thus attractive within the well-established crystalline silicon solar cell process flow.

Acknowledgments

The authors would like to thank the National Science Foundation, the Silicon Solar Consortium (SiSoC), our industrial mentor DuPont, and North Carolina State University.

4. References

1. Trinnaman, J.; Clarke, A.; Council, W. E., *2004 Survey of Energy Resources*. 20 ed.; Elsevier: Amsterdam, 2004.

2. Interior, U. S. D. o. t.; Survey, U. S. G., The U.S. Geological Survey Energy Resources Program. **2010**.

3. How Solar Electric Technology Works. http://www.solardirect.com/pv/pvbasics/pvbasics.htm.

4. Photovoltaics, N. N. C. f. http://www.nrel.gov/ncpv/ (accessed July 12, 2012).

5. Einstein, A., Annus Mirabilis papers. *Annalen der Physik* **1905**.

6. Reference Solar Spectral Irradiance: Air Mass 1.5. http://rredc.nrel.gov/solar/spectra/am1.5/.

7. Laboratory, N. N. R. E. Dynamic Maps, GIS Data, & Analysis Tools. http://www.nrel.gov/gis/solar.html/.

8. Neville, R. C., *Solar energy conversion: the solar cell*. 2 ed.; Elsevier: Amsterdam, 1995.

9. Hummel, R. E., *Electronic Properties of Materials*. 3 ed.

10. Tilley, R., *Understanding Solids*. John Wiley & Sons, Ltd.: Hoboken, NJ, 2004.

11. Griffiths, D. J., *Introduction to Quantum Mechanics*. 2 ed.; Pearson Education, Inc.: 2005.

12. Fan, W. J.; Xia, J. B.; Agus, P. A.; Tan, S. T.; Yu, S. F., Band parameters and electronic structures of wurtzite ZnO and ZnO/MgZnO quantum wells. *Journal of Applied Physics* **2006,** *99*.

13. Lang, D. V., Deep-level transient spectroscopy: A new method to characterize traps in semiconductors. *Journal of Applied Physics* **1974,** *45* (7).

14. Askerov, B. M., *Electron Transport Phenomena in Semiconductors*. 1985.

15. Photovoltaics Research. http://www.nrel.gov/pv/advanced_concepts.html.

16. Sundaram, K. B.; Khan, A., Work function determination of zinc oxide films. *J. Vac. Sci. Technol. A* **1997,** *15*, 428-430.

17. Granqvist, C. G., Transparent conductors as solar energy materials: A panoramic review. *Solar Energy Materials & Solar Cells* **2007,** (91).

18. Fill Factor. http://www.pveducation.org/pvcdrom/solar-cell-operation/fill-factor.

19. SolarOne Learning Center. http://www.solarone.net.

20. Shockley, W.; Queisser, H. J., Detailed Balance Limit of Efficiency of pn Junction Solar Cells. *J. Appl. Phys.* **1961,** *32*, 510-519.

21. Vos, A. D., Detailed balance limit of the efficiency of tandem solar cells. *J. Phys. D: Appl. Phys.* **1980,** *13*, 839-46.

22. SMECC Carl Zeiss - A History of a Most Respected Name in Optics. http://www.smecc.org/ziess.htm.

23. This Month in Physics History. *APS News* 2007.

24. Macleod, H. A., *Thin-Film Optical Filters*. 3 ed.; Taylor & Francis: 2001.

25. Hovel, H. J., *Semiconductors and Semimetals*. Academic Press: New York, 1975; Vol. 11.

26. Raut, H. K.; Ganesh, V. A.; Nair, A. S.; Ramakrishna, S., Anti-reflective coatings: A critical, in-depth review. *Energy & Environmental Science* **2011,** *4*, 3779-3804.

27. Vukusic, P., Natural photonics. *Physics World* **2004**.

28. Min, W.-L.; Betancourt, A. P.; Jiang, P.; Jiang, B., Bioinspired broadband antireflection coatings on GaSb. *Applied Physics Letters* **2008,** *92*, 141109.

29. Kishore, R.; Singh, S. N.; Das, B. K., PECVD grown silicon nitride AR coatings on polycrystalline silicon solar cells. *Solar Energy Materials & Solar Cells* **1992,** *26*, 27-35.

30. Sopori, B., Silicon Nitride Processing for Control of Optical and Electronic Properties of Silicon Solar Cells. *Journal of Electronic Materials* **2003,** *32* (10), 1034-1042.

31. Fortunato, E.; Ginley, D.; Hosono, H.; Paine, D. C., Transparent Conducting Oxides for Photovoltaics. *MRS Bulletin* **2007,** *32*, 242-247.

32. Indium Oxide and Indium-Tin Oxide (ITO) Coatings. America, I. C. o., Ed.

33. Zafar, S.; Ferekides, C. S.; Morel, D. L., *J. Vac. Sci. Technol. A* **1995,** *13* (4), 2177.

34. (a) Fathollahi, V.; Amini, M. M., Sol-gel preparation of highly oriented gallium-doped zinc oxide thin films. *Materials Letters* **2001,** *50*, 235-239; (b) Ilican, S.; Caglar, Y.; Caglar, M., Preparation and characterization of ZnO thin films deposited by sol-gel spin coating method. *Journal of Optoelectronics and Advanced Materials* **2008,** *10* (10), 2578-2583.

35. Robbins, J. J.; Harvey, J.; Leaf, J.; Fry, C.; Wolden, C. A., Transport phenomena in high performance nanocrystalline ZnO:Ga films deposited by plasma-enhanced chemical vapor deposition. *Thin Solid Films* **2005,** *473*, 35-40.

36. (a) Kim, C. E.; Moon, P.; Yun, I.; Kim, S.; Myoung, J.-M.; Jang, H. W.; Bang, J., Process estimation and optimized recipes of ZnO:Ga thin film characteristics for transparent electrode applications. *Expert Systems with Applications* **2011,** *38*, 2823-2827; (b) Park, S. E.; Lee, J. C.; Song, P. K.; Lee, J.-H., Properties of Gallium-Doped Zinc-Oxide Films Deposited by RF or DC Magnetron Sputtering with Various GZO Targets. *Journal of the Korean Physical Society* **2009,** *54* (3), 1283-1287.

37. (a) Tripathi, S.; Choudhary, R. J.; Tripathi, A.; Baranwal, V.; Pandey, A. C.; Gerlach, J. W.; Dar, C.; Kanjilal, D., Studies of effect of deposition parameters on the ZnO films prepared by PLD. *Nuclear Instruments and Methods in Physics Research B* **2008,** *266*; (b) Fan, X. M.; Lian, J. S.; Jiang, Q.; Zhou, Z., Effect of the oxygen pressure on the photoluminescence properties of ZnO thin films by PLD. *J. Mater. Sci.* **2007**; (c) Wei, X. Q.; Zhang, Z.; Yu, Y. X.; Man, B. Y., Comparative study on structural and optical properties of ZnO thin films prepared by PLD using ZnO powder target and ceramic target. *Optics & Laser Technology* **2009,** *41*, 530-534; (d) Henley, S. J.; Ashfold, M. N. R.; Cherns, D., The growth of transparent conducting ZnO films by pulsed laser ablation. *Surface and Coatings Technology* **2004,** *177*, 271-276; (e) Park, S.-M.; Ikegami, T.; Ebihara, K., Effects of substrate temperature on the properties of Ga-doped ZnO by pulsed laser deposition. *Thin Solid Films* **2006,** *513*, 90-94.

38. Li, Y.-Q.; Yong, K.; Xiao, H.-M.; Ma, W.-J.; Zhang, G.-L.; Fu, S.-Y., Preparation and electrical properties of Ga-doped ZnO nanoparticles by a polymer pyrolysis method. *Materials Letters* **2010,** *64*, 1735-1737.

39. Janotti, A.; Walle, C. G. V. d., Fundamentals of zinc oxide as a semiconductor. *Reports on Progress in Physics* **2009,** *72*.

40. Chemexplore. http://www.chemexplore.net/antifluorites.htm.

41. Kim, Y.; Lee, W.; Jung, D.-R.; Kim, J.; Nam, S.; Kim, H.; Park, B., Optical and electronic properties of post-annealed ZnO:Al thin films. *Applied Physics Letters* **2010,** (96).

42. Krebs, H.-U.; Weisheit, M.; Faupel, J.; Suske, E.; Scharf, T.; Fuhse, C.; Stormer, M.; Sturm, K.; Seibt, M.; Kijewski, H.; Nelke, D.; Panchenko, E.; Buback, M., Pulsed Laser Deposition (PLD) - a Versatile Thin Film Technique.

43. Pulsed Laser Deposition (PLD) of thin films. http://ap.polyu.edu.hk/apakhwon/lecture_notes/Thin_Films3.pdf.

44. Morkoc, H.; Ozgur, U., *Zinc Oxide: Fundamentals, Materials and Device Technology*. John Wiley & Sons: 2008.

45. (a) Yelundur, V.; Nakayashiki, K.; Hilali, M.; Rohatgi, A., Implementation of a Homogeneous High-Sheet-Resistance Emitter in Multicrystalline Silicon Solar Cells. *IEEE* **2005**; (b) Schroder, D. K.; Meier, D. L., Solar Cell Contact Resistance - A Review. *IEEE Transactions on Electron Devices* **1984,** *31* (5).

46. *SiC Materials and Devices*. Academic Press: Arlington, VA, 1998; Vol. 52.

47. Yu, C.-F.; Chen, S.-H.; Sun, S.-J.; Chou, H., Influence of the grain boundary barrier height on the electrical properties of Gallium doped ZnO thin films. *Applied Surface Science* **2011,** *257*, 6498-6502.

48. (a) Chang, C. Y.; Fang, Y. K.; Sze, S. M., Specific Contact Resistance of Metal-Semiconductor Barriers. *Solid-State Electronics* **1971,** *14*, 541-550; (b) Yu, A. Y. C., Electron Tunneling and Contact Resistance of Metal-Silicon Contact Barriers. *Solid-State Electronics* **1970,** *13*, 239-247.

49. Yim, K.; Kim, H. W.; Lee, C., Effects of annealing on structure, resistivity and transmittance of Ga doped ZnO films. *Materials Science and Technology* **2007**.

50. Liu, Z. W.; Fu, W. J.; Liu, M.; Gu, J. F.; Ma, C. Y.; Zhang, Q. Y., Scaling behavior and coarsening transition of annealed ZnO films on Si substrate. *Surface and Coatings Technology* **2008,** *202*, 5410-5415.

51. Olorunyolemi, T.; Tolbert, R.; Jr., O. W.; Carmel, Y.; Lloyd, I.; Xu, G.; Jaworski, A., Measurement of Densification of Zinc Oxide Compacts Using an Optical, Noncontact, Noninvasive Extensometer. *J. Am. Ceram. Soc.* **2000,** *83* (4), 974-976.

52. Ichinose, N., *Introduction to Fine Ceramics*. John Wiley & Sons LTD: New York, NY, 1987.

53. Kern, W., Handbook of Semiconductor Wafer Cleaning Technology. Science, T., and Applications, Ed. Werner Kern Associates: East Windsor, New Jersey, 1993.

54. Filho, S. G. d. S.; Hasenack, C. M.; Salay, L. C.; Mertens, P., A Less Critical Cleaning Procedure for Silicon Wafer Using Diluted HF Dip and Boiling in Isopropyl Alcohol as Final Steps. *J. Electrochem. Soc.* **1995,** *142* (3).

55. Lift-off Processes with Photoresists. http://www.microchemicals.eu/technical_information/lift_off_photoresist.pdf.

56. Hilali, M. M.; Al-Jassim, M. M.; To, B.; Moutinho, H.; Rohatgi, A.; Asher, S., Understanding the Formation and Temperatuer Dependence of Thick-Film Ag Contacts on High-Sheet-Resistance Si Emitters for Solar Cells. *Journal of the Electrochemical Society* **2005,** *152* (10).

57. (a) Kundu, S.; Hazra, S.; Banerjee, S.; Sanyal, M. K.; Mandal, S. K.; Chaudhurl, S.; Pal, A. K., Morphology of thin silver film grown by dc sputtering on Si(001). *J. Phys. D: Appl. Phys.* **1998,** *31*; (b) Marechal, N.; Quesnel, E.; Pauleau, Y., Silver thin films deposited by magnetron sputtering. *Thin Solid Films* **1994,** *241*, 34-38.

58. Phani, A. R.; Santucci, S.; Nardo, S. D.; Lozzi, L.; Passacantando, M.; Picozzi, P., Preparation and characterization of bulk ZnGa2O4. *Journal of Materials Science* **1998,** *33*, 3969-3973.

59. (a) Sze, S. M., *Semiconductor Devices: Physics and Technology*. 2 ed.; John Wiley & Sons, Inc: 1985; (b) Schroder, D. K., *Semiconductor Material And Device Characterization*. 3 ed.; John Wiley & Sons: 2006.

60. The van der Pauw Technique. http://tau.nanophys.kth.se/cmp/hall/node5.html.

61. (a) Fujiwara, H.; Kondo, M., Effects of carrier concentration on the dielectric function of ZnO:Ga and In2O3:Sn studied by spectroscopic ellipsometry: Analysis of free-carrier and band-edge absorption. *Physical Review B* **2005,** *71*; (b) Dai, Z.-H.; Zhang, R.-J.; Shao, J.; Chen, Y.-M.; Zheng, Y.-X.; Wu, J.-D.; Chen, L.-Y., Optical Properties of Zinc-oxide Films Determined Using Spectroscopic Ellipsometry with Various Dispersion Models. *Journal of the Korean Physical Society* **2009,** *55* (3), 1227-1232; (c) Liu, Y. C.; Hsieh, J. H.; Tung, S. K., Extraction of optical constants of zinc oxide thin films by ellipsometry with various models. *Thin Solid Films* **2006,** *510*, 32-38.

62. (a) Berger, H. H., Contact Resistance and Contact Resistivity. *J. Electrochem. Soc.: Solid-State Science and Technology* **1972,** *119* (4); (b) Sawdai, D.; Pavlidis, D.; Cui, D., Enhance Transmission Line Model Structures for Accurate Resistance Evaluation of Small-Size Contacts and for More Reliable Fabrication. *IEEE Transactions on Electron Devices* **1999,** *46* (7).

63. Vinod, P. N., Specific contact resistance measurements of the screen-printed Ag thick film contacts in the silicon solar cells by three-point probe methodology and TLM method. *Journal of Materials Sciences: Materials Electronics* **2011,** *22*.

64. Stavitski, N.; Dal, M. J. H. v.; Wolters, R. A. M.; Kovalgin, A. Y.; Schmitz, J., Specific Contact Resistance Measurements of Metal-Semiconductor Junctions.

65. Klootwijk, J. H.; Timmering, C. E., Merits and Limitations of Circular TLM structures for contact resistance determination for novel III-V HBTs. *Proc. IEEE 2004 Int. Conference on Microelectronic Test Structures* **2004,** *17*.

66. Gallacher, K.; Velha, P.; Paul, D. J.; MacLaren, I.; Myronov, M., Ohmic contacts to n-type germanium with low specific contact resistivity. *Applied Physics Letters* **2012,** *100*.

67. (a) Kato, H.; Umezawa, H.; Tokuda, N.; Takeuchi, D.; Okushi, H., Low specific contact resistance of heavily phosphorus-doped diamond film. *Applied Physics Letters* **2008,** *93*; (b) Yang, H. S.; Li, Y.; Norton, D. P.; Ip, K.; Pearton, S. J., Low-resistance ohmic contacts to p-ZnMgo grown by pulsed-laser deposition. *Applied Physics Letters* **2005,** *86*.

68. Stareev, G.; Kunzel, H.; Dortmann, G., A controllable mechanism of forming extremely low resistance nonalloyed ohmic contacts to group III-V compound semiconductors. *J. Appl. Phys.* **1993,** *74*.

69. Chen, J.-J.; Jang, S.; Anderson, T. J.; Ren, F.; Li, Y., Low specific contact resistance Ti/Au contacts on ZnO. *Applied Physics Letters* **2006,** *88*.

70. Ebong, A.; Rounsaville, B.; Cooper, I. B.; Tate, K.; Upadhyaya, A.; Rohatgi, A., Optimizing the Inline Emitters for Higher Efficiency Silicon Solar Cells.

71. (a) Kim, D. W.; Sung, Y. J.; Park, J. W.; Yeom, G. Y., A study of transparent indium tin oxide (ITO) contact to p-GaN. *Thin Solid Films* **2001**, 87-92; (b) Cheng, Y.-T.; Ho, J.-J.; Wang, C.-K.; Lee, W.; Lu, C.-C.; Yau, B.-S.; Nain, J.-L.; Chang, S.-H.; Chang, C.-C.; Wang, K. L., Improvement of organic solar cells by flexible substrate and ITO surface treatments. *Applied Surface Science* **2010,** *256*, 7606-7611.

72. Demchenko, D. O.; Earles, B.; Liu, H. Y.; Avrutin, V.; Izyumskaya, N.; Ozgur, U.; Morkoc, H., Impurity complexes and conductivity of Ga-doped ZnO. *Physical Review B* **2011,** *84* (075201).

73. (a) Yim, K.; Lee, C., Dependence of the electrical and optical properties of sputter-deposited ZnO:Ga films on the annealing temperature, time, and atmosphere. *J. Mater Sci: Mater Electron* **2007,** *18*, 385-390; (b) Lee, J.-H.; Ko, K.-H.; Park, B.-O., Electrical and optical properties of ZnO transparent conducting films by the sol–gel method. *Journal of Crystal Growth* **2003,** *247*, 119-125.

74. Polyanskiy, M. RefractiveIndex.INFO Refractive index database. refractiveindex.info.

75. (a) Sheu, J. K.; Shu, K. W.; Lee, M. L.; Tun, C. J.; Chi, G. C., Effect of Thermal Annealing on Ga-Doped ZnO Films Prepared by Magnetron Sputtering. *Journal of the Electrochemical Society* **2007,** *6* (154); (b) Walsh, A.; Silva, J. L. F. D.; Wei, S.-H., Origins of band-gap renormalization in degenerately doped semiconductors. *Physical Review B* **2008,** *78*; (c) Burstein, E., Anomalous Optical Absorption Limit in InSb. *Physical Review* **1954,** *93* (3), 632-633; (d) Moss, T. S., The interpretation of the properties of indium antimonide. *Proc. Phys. Soc. London B* **1954,** *67*, 775-782.

APPENDIX

APPENDIX

This appendix contains experimental results which were not necessary for the manuscript, but which deserve preservation.

A.1 Optimization of Dopant Concentration, wt% Ga

As discussed, doping of ZnO is an easy way to change the optical and electrical properties of ZnO thin films. Left undoped, ZnO has a direct band gap of 3.37 eV at room temperature and a large exciton binding energy of 60 meV. By doping ZnO with a group III element, the material becomes an n-type semiconductor by substitution of group III elements for Zn atoms. The system also relies on vacant oxygen sites to create charge carriers. These sites are optically active, and dopant substitution makes oxygen loss less favorable. Gallium was chosen as the dopant for many reasons. Its abundance makes it cheaper than indium, and its atomic size matches that of zinc better than aluminum, causing less lattice distortion and thus less stress. As gallium is added to the undoped ZnO, electrical properties improve until a critical point, at which further doping decreases the conductivity of the material, as there are no longer zinc substitutions to be made or interstitials to be filled, and the excess gallium is a detriment.

This section investigates where this critical doping amount lies, and how various optoelectronic characteristics are affected by the dopant concentration. Different targets were made, with 0, 1, 2, 3, 4, and 5 wt% Ga content in the ZnO powder. The targets were observed by X-ray diffraction to examine elemental composition. Then,

thin films were deposited by PLD with each different target. UV-vis spectroscopy was performed to examine %Transmission. Hall measurements, 4-point probe measurements, and profilometry were performed to measure resistivity as a function of dopant concentration. The following section reports the results from these experiments, and determines the optimal dopant concentration to use for further experimentation.

It will be shown that optimal conductivity occurs with 1 wt% Ga doping. From the UV-vis spectroscopy measurements, we will observe a shift in wavelength consistent with the onset of a second, spinel phase. We will see that 90% or better transmission is achieved for the 400-800nm wavelength range, regardless of the dopant concentration used.

A.1.1 Structural Characterization by XRD

To examine the structural changes of the pressed and sintered ceramic targets as a function of dopant concentration, X-ray diffraction measurements were performed to visualize the evolution of the diffraction peaks.

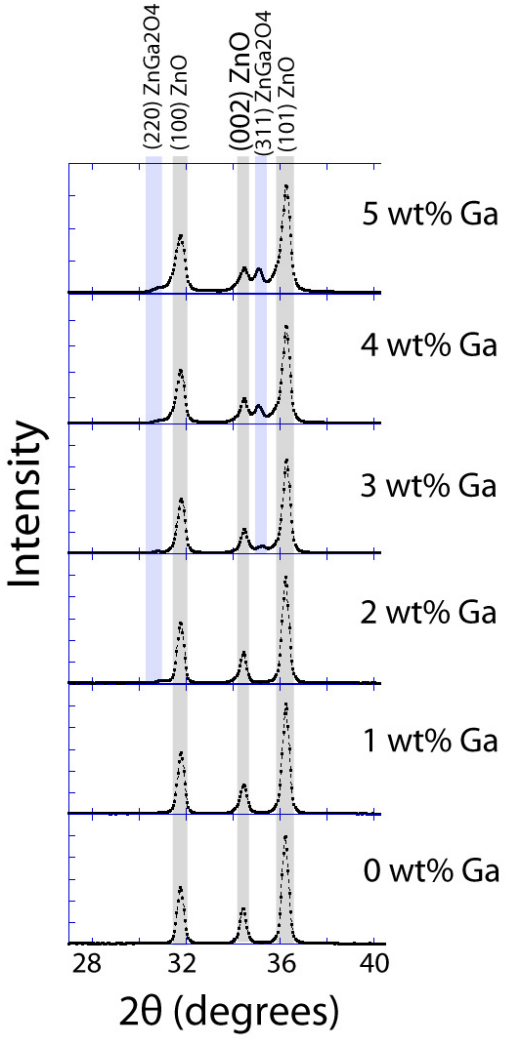

Figure 28 XRD data of GZO pellets with various amounts of Ga dopant

The consistency of the (002) peaks indicate that Ga doping did not cause structural degradation of the wurtzite ZnO structure[37e]. The appearance of the $ZnGa_2O_4$ peaks indicates that there is a spinel phase formation above 2 wt% Ga. Instead of observing Zn substitution and vacant oxygen sites in the hexagonal wurtzite ZnO structure with

tetrahedrally coordinated zinc atoms, the crystal structure undergoes a transformation to an alternative crystal structure, the spinel, crystallizing in the cubic crystal system, thus giving rise to the possibility of changes in the electrical and optical properties, which will be examined in sections 4.1.2 and 4.1.3.

A.1.2 Optical characterization by UV-vis spectroscopy

As the main purpose of creating a thin film of GZO is the form an anti-reflective coating (ARC), it is important to characterize the films by how much light is transmitted through the film. To examine the dependence of transmission on dopant concentration, 1 μm thick films were pulsed laser deposited onto cleaned glass substrates using each of the variously doped targets. UV-vis spectroscopy was used to measure percent transmission as a function of wavelength of the incoming light, and each were compared, as can be seen in Figure 29.

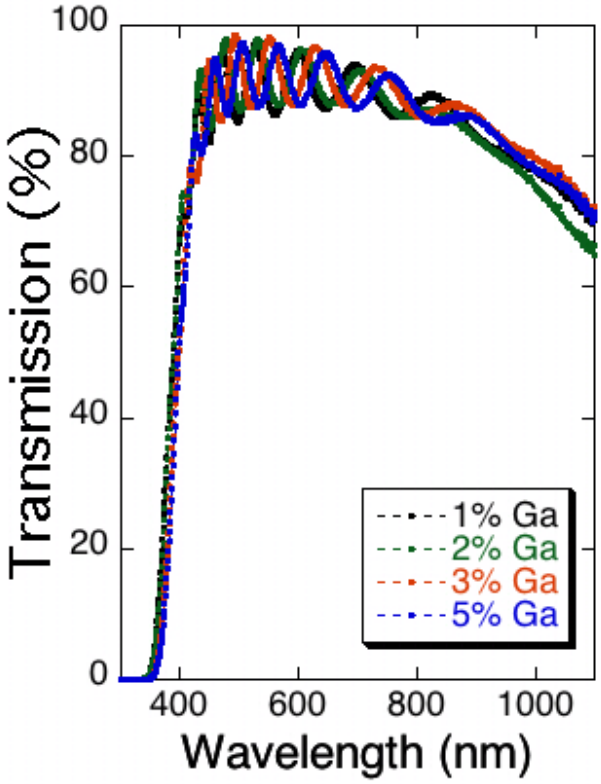

Figure 29 Transmission vs. Wavelength of 1 μm thick GZO films of various dopant concentrations. The decline in transmission at the longer wavelengths approaching the IR is not present in thinner films, as will be seen later.

It appears that for the bulk of the visible wavelength, namely from 500-800 nm wavelengths, transmission is independent of dopant concentration. At the lower wavelengths, around 350-450 nm, the onset of transmission can be seen to have a dependence on dopant concentration. Figure 30 shows a close-up of the short wavelength range.

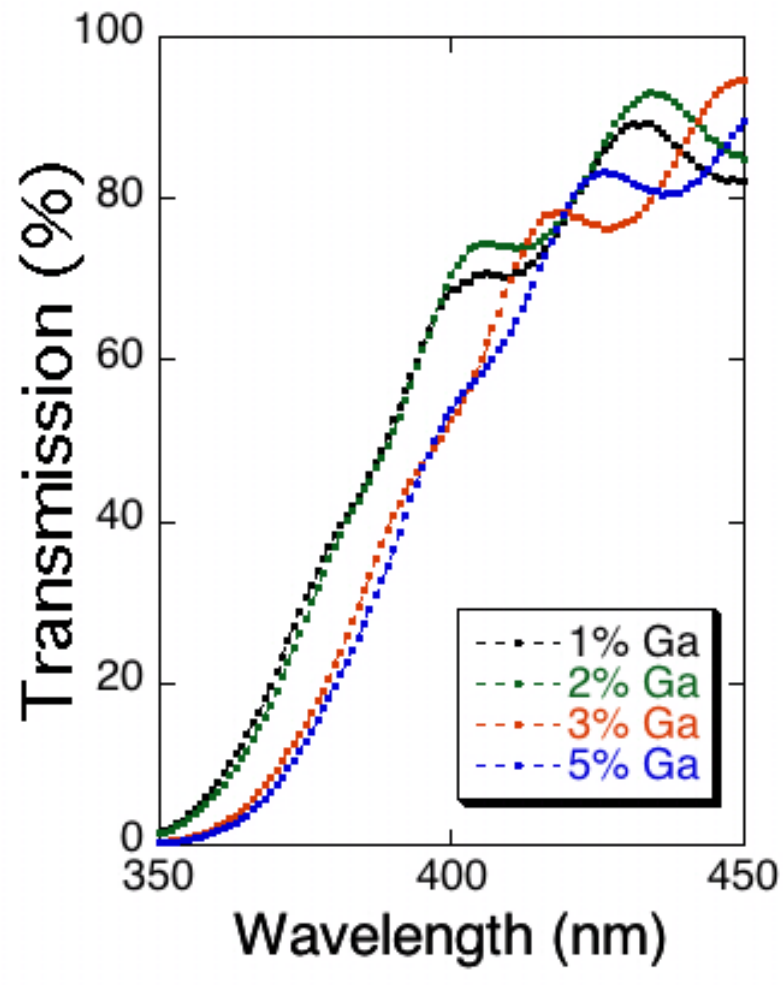

Figure 30 Transmission vs. Wavelength for the short wavelength range

There is a drop in transmission between 2 and 3 wt% gallium dopant. This is consistent with the onset of the second phase (the spinel phase) present in the target compositions. Fortunately, the targets that yield films with the widest transparency range also yield the lowest resistivity films, as will be shown in next section. The loss of transmission at longer wavelengths is due to the Burstein-Moss effect[61a, 75]. As carrier

concentration increases, the absorption edge is shifted to higher energies. When doping becomes degenerate, carriers have to be promoted to higher energies in order to find unoccupied energy levels, and thus the shift occurs.

Nevertheless, this shift does not have a significant bearing on the overall spectrum of transmitted light, and thus transparency is not a limiting factor in determining which dopant concentration is ideal to optimize optoelectronic properties of our thin film.

A.1.3 Electrical characterization by Hall effect and 4-point probe

This section explores electrical characterization as a function of dopant concentration. Films of 200nm thickness were deposited using targets of varying dopant concentration, and the resistivity of each film was measured using two methods: (1) profilometry and four-point probe measurements, and (2) Hall effect measurements. The results are shown in Figure 31.

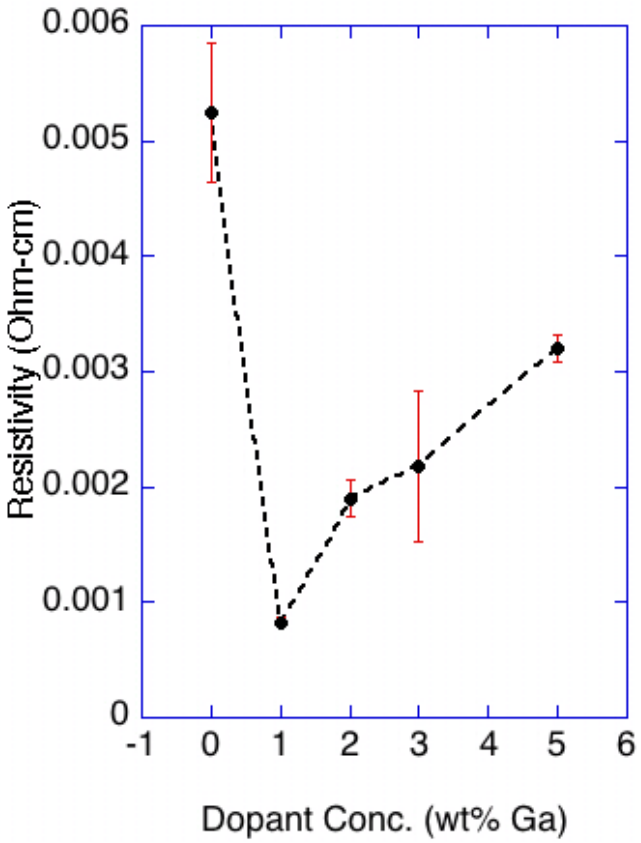

Figure 31 Resistivity vs. dopant concentration. Measurements were made by 4-point probe and by the Hall effect method. The data points are from 4-point probe measurements, and the error bars correspond to Hall effect measurements.

From the figure, we see that the minimum resistivity occurs using 1 wt% Ga doping in our GZO films. As this composition gives us the optimal resistivity measurements as well as phase pure films (no spinel phase present), 1 wt% doping is deemed ideal and is used for the remainder of the experiments.

A.2 Atomic force microscopy (AFM) of GZO as a function of O_2 pressure

AFM has been performed on 1 wt% Ga doped ZnO grown at different deposition pressures, and the results are comparable to results shown on undoped ZnO[37b].

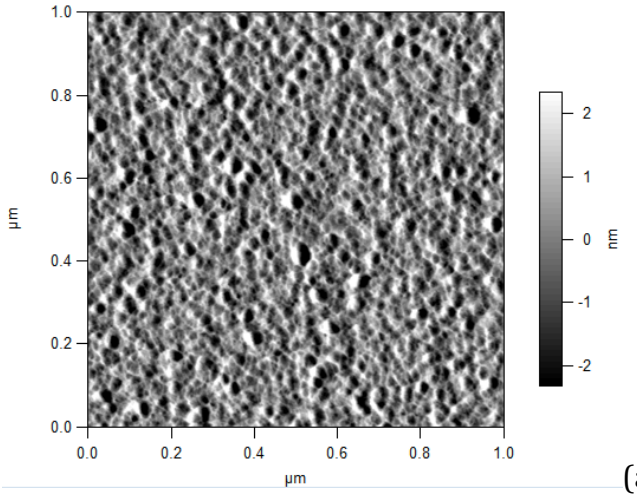
1.0
0.8
0.6
0.4
0.2
0.0
µm
0.0
0.2
0.4
0.6
0.8
1.0
µm
2
1
0
-1
-2
nm

(a)

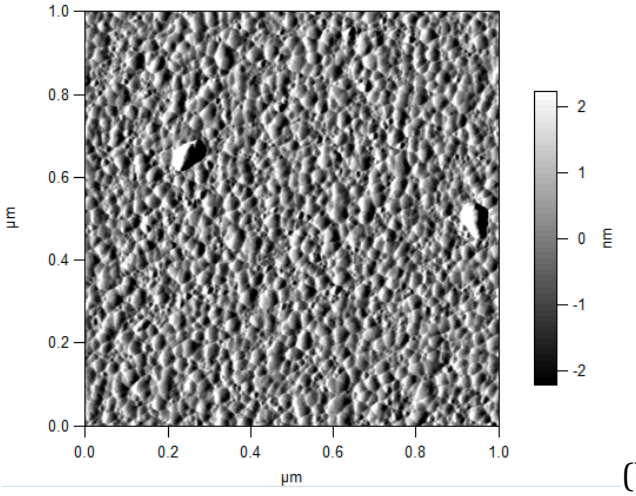
1.0
0.8
0.6
0.4
0.2
0.0
µm
0.0
0.2
0.4
0.6
0.8
1.0
µm
2
1
0
-1
-2
nm

(b)

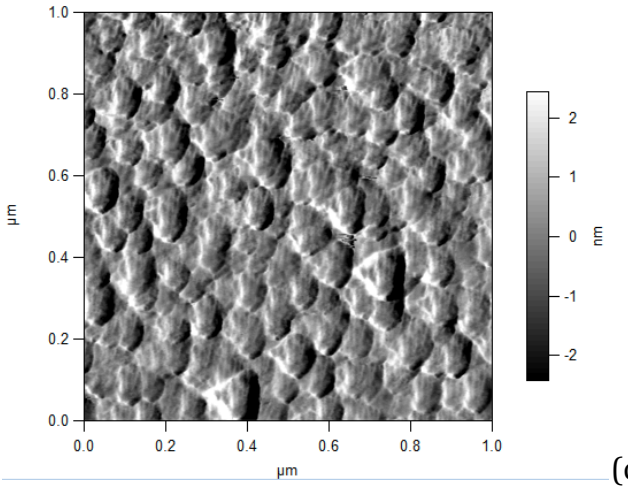
1.0
0.8
0.6
0.4
0.2
0.0
µm
0.0
0.2
0.4
0.6
0.8
1.0
µm
2
1
0
-1
-2
nm

(c)

Figure 32 AFM images of 1 wt% Ga-doped ZnO at O_2 deposition pressures of (a) 1 mTorr, (b) 5 mTorr, and (c) 30 mTorr

From these images, it is apparent that grain size grows as deposition pressure is increased.

A.3 Optimization of Film Thickness

Optimizing film thickness is an important parameter for achieving antireflection. To determine optimal film thickness, UV-vis measurements were taken using an integrating sphere to observe transmission and reflection properties of GZO films on glass substrates and monocrystalline, textured solar cells, respectively.

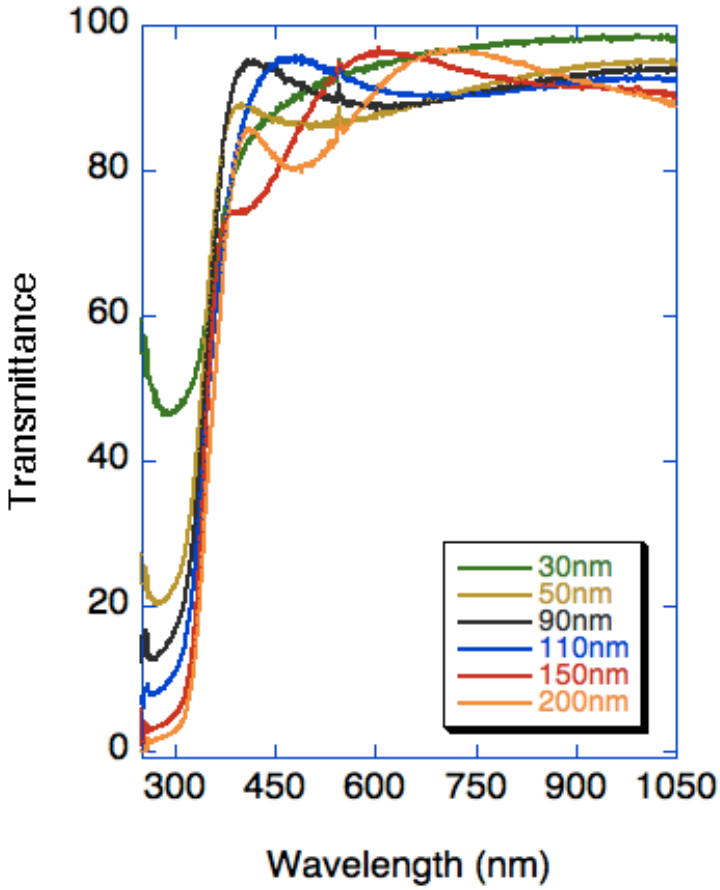

Figure 33 Transmission vs. Wavelength data for GZO films on glass substrates. The GZO films range from 30nm to 200nm in thickness

The transmission data in Figure 33 shows that all films from 30nm to 200nm have suitable transmissive properties (90%+), with no fall-off at high wavelength ranges.

Reflection data is shown in the manuscript in section 3.

A.4 Investigation of Refractive Index

Bulk ZnO is known to have a refractive index in the proper range to interface air and silicon media. Air has a refractive index of 1, and silicon a refractive index of 3.4. We want to confirm that GZO also has a suitable refractive index. Figure 34 shows the results of ellipsometry measurements on 90nm thick GZO on a smooth Si substrate. Each of the three films was deposited at a different oxygen pressure.

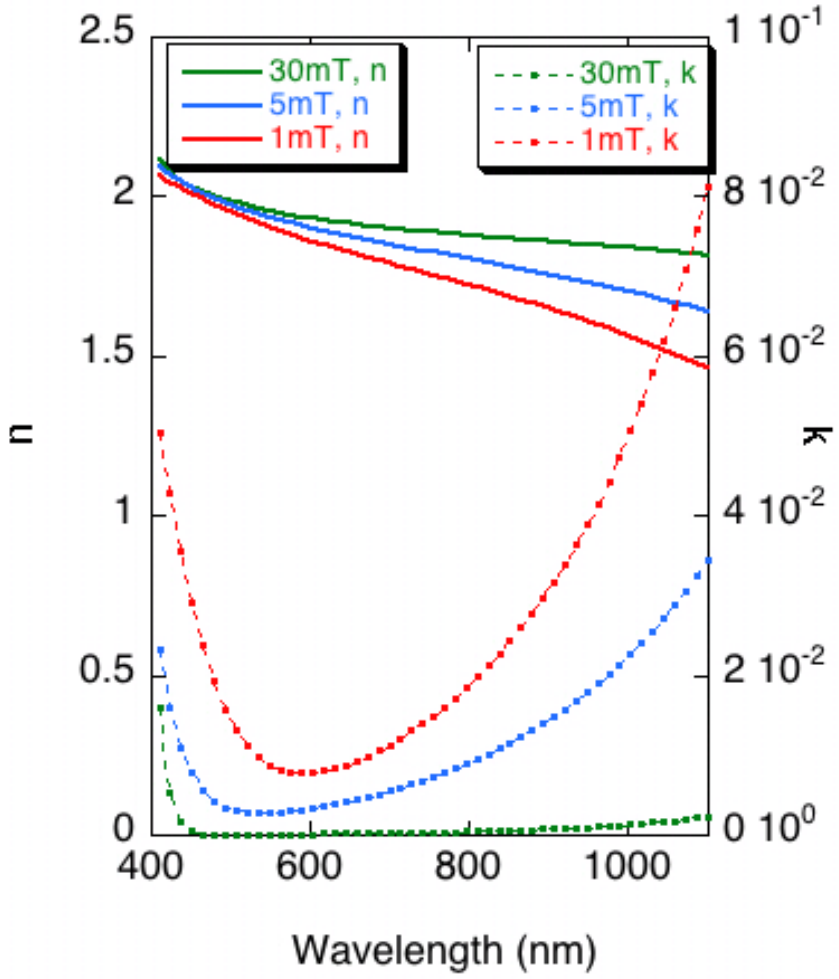

Figure 34 Refractive index and absorption coefficient vs. wavelength of 90nm thick GZO films deposited at 1, 5, and 30 mTorr of oxygen pressure during PLD

The model used to map the above real and imaginary refractive indices is absorbing in the infrared (metal-like), and absorbing before the band gap edge (around 380nm). The dependence of refractive index on deposition pressure is consistent with the Hall measurement results from Section 3. There are fewer charge carriers when deposited in high O_2 pressures, and thus these films are less absorbing. Literature results for refractive index of Ga-doped ZnO show similar results[61a].